Fluvial or aeolian? Unravelling the origin of the silty clayey sediment cover of terraces in the Hanzhong Basin (Qinling Mountains, central China)

van Buuren, Unze; Prins, Maarten A.; Wang, Xianyan; Stange, Martin; Yang, Xun; van Balen, Ronald T.

published in
Geomorphology
2020

DOI (link to publisher)
10.1016/j.geomorph.2020.107294

document version
Publisher's PDF, also known as Version of record

Geomorphology 367 (2020) 107294

Contents lists available at ScienceDirect

Geomorphology

journal homepage: www.elsevier.com/locate/geomorph

Fluvial or aeolian? Unravelling the origin of the silty clayey sediment cover of terraces in the Hanzhong Basin (Qinling Mountains, central China)

Unze van Buuren [a,*], Maarten A. Prins [a], Xianyan Wang [b], Martin Stange [c], Xun Yang [b], Ronald T. van Balen [a,d]

[a] Earth and Climate Cluster, Dep. Earth Sciences, Vrije Universiteit Amsterdam, the Netherlands
[b] School of Geography and Ocean Science, Nanjing University, China
[c] Fachbereich Geowissenschaften der Universität Bremen, Germany
[d] TNO Geologische Dienst Nederland, Utrecht, the Netherlands

ARTICLE INFO

Article history:
Received 27 February 2019
Received in revised form 3 June 2020
Accepted 3 June 2020
Available online 18 June 2020

Keywords:
Depositional environment
Grain size
Grain shape
Fluvial
Aeolian
End-member modelling

ABSTRACT

This study is focused on a silty clayey sedimentary sequence on a terrace in the intramontane Hanzhong Basin, located in the Qinling Mountains (QLM), central China. Traditionally, the QLM are considered to have blocked dust transport from northwest to southeast China. However, in recent years, geo-archaeological studies have documented loess-palaeosol sequences at numerous locations in and surrounding the QLM. In the loess deposits overlying the terraces of the Hanjiang River in the Hanzhong-, Ankang- and Yunxian basins, abundant artefacts, flakes, stone tools (e.g., scrapers and choppers) and cores are commonly found. The loess deposits have been deposited with lower sedimentation rates, and they are finer grained and more intensely weathered compared to the loess deposits on the Central Loess Plateau (CLP). The loess deposits overly coarse sandy and gravely fluvial deposits (terraces). Silty fluvial deposits are situated in between them. Discrimination between these two types of deposits could prove difficult because both deposits are fine grained (silt and clay) and can have similar grain size distribution characteristics. This is, however, crucial for palaeo-environmental interpretations during hominin occupation, understanding fluvial morphodynamics, and for pedostratigraphic correlation with the typical loess-palaeosol sequences on the CLP. The aim of this research is to determine and characterize the transition of the fluvial to aeolian depositional environment in a fine grained sequence, based on field observations, organic matter and carbonate content, grain size and shape analyses, mineral content (mica's) and end-member modelling of the grain size dataset. In addition, terrestrial cosmogenic nuclides (TCN) burial dating is used to determine the age of the basal, coarse grained fluvial deposits. The determined age, 0.6 ± 0.14 Ma, allows for a chronological correlation of the deposits to the loess-palaeosol sequence on the CLP independent from the pedostratigraphic correlation. This age also gives insight in terrace abandonment and the fluvial morphodynamics of the Hanjiang River.

The result indicates a clear distinction between sediments deposited in a fluvial environment and those formed in an aeolian depositional environment. However, the aeolian (loess) deposits show some atypical characteristics. For example, the end-member model results show a coarsening in the five palaeosol layers. This is in contrast with the fine grained nature of palaeosols on the CLP. The coarsening observed in the studied palaeosol layers is interpreted as the result of local surface runoff processes, eroding fine sediment and/or depositing relatively coarse material during interglacial periods.

Because of the known depth of the fluvial-aeolian transition and the absolute age of the TCN burial dated terrace deposits, pedostratigraphic correlation of the palaeosol layers with the Central Loess Plateau is possible. The oldest palaeosol is correlated with S5 (0.625–0.503 Ma). The transition from a fluvial to aeolian environment takes place in L6, between 0.625 and 0.693 Ma. This is consistent with the TCN age of 0.6 ± 0.14 Ma. This age also marks the abandonment of the terrace caused by incision of the Hanjiang River, which is possibly related to an uplift phase of the QLM.

1. Introduction

The Qinling Mountains (QLM, Fig. 1A) are situated at the climatic boundary between the semiarid north and the subtropical south in

* Corresponding author at: Department of Earth Sciences, Faculty of Science, Vrije Universiteit Amsterdam, De Boelelaan 1085, 1081 HV Amsterdam, the Netherlands.
E-mail address: u.van.buuren@vu.nl (U. van Buuren).

https://doi.org/10.1016/j.geomorph.2020.107294
0169-555X/

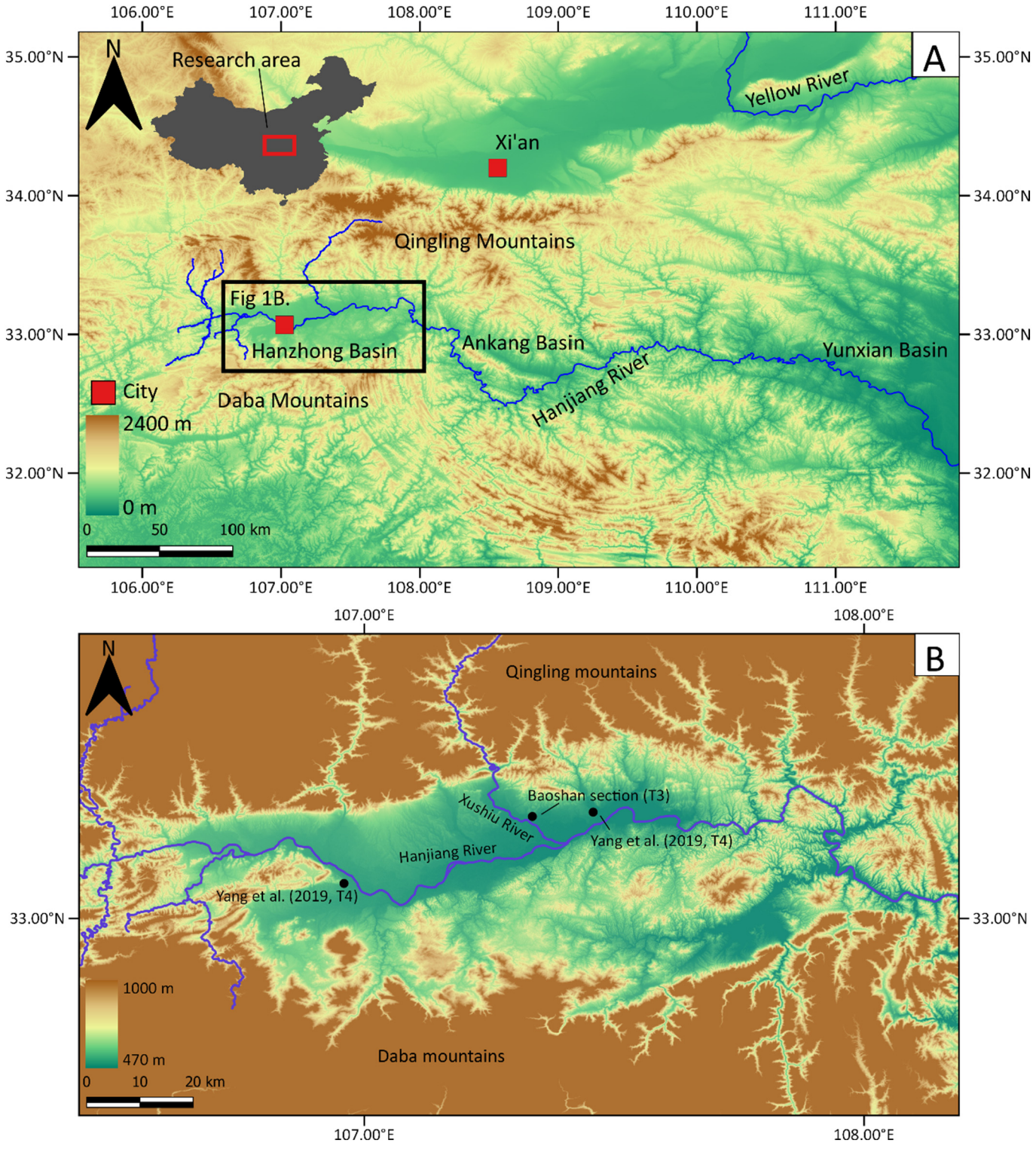

Fig. 1. (A) Digital elevation model (DEM) of Central China with the intramontane Hanzhong-, Ankang-, and Yunxian basins. The area of the DEM is highlighted with a red box in the inset map of China. The research area (the Hanzhong Basin) is indicted with the black rectangle. (B) The Hanzhong Basin is located in between the Qinling mountains and the Daba Mountains. The location of the Baoshan section and sites studied by Yang et al. (2019) are indicated with black dots.

central China. Traditionally, the QLM were considered to have partly blocked dust transport from northwest to southeast China (Zhang et al., 2012). However, in recent years, geo-archaeological studies have documented loess-palaeosol sequences at numerous locations in and surrounding the QLM. In the loess deposits overlying the terraces of the Hanjiang River in the Hanzhong, Ankang and Yunxian basins abundant artefacts, flakes, stone tools (e.g., scrapers and choppers) and cores are commonly found (Sun et al., 2017b), but also in adjoining areas, like Lantian, and the Luonan and Lushi basins (Lu et al., 2011a, 2011b; Sun et al., 2014; Wang et al., 2014). Pedostratigraphic correlation of the loess deposits on the terraces with the well-dated loess-palaeosol sequence on the Central Loess Plateau (CLP), located to the north of the QLM, significantly contributed to the chronology and natural environment reconstructions for hominins (Lu et al.,

2011a, 2011b; Zhang et al., 2012; Sun et al., 2013, 2014, 2017b; Fang et al., 2017).

The loess-palaeosol sequences in and around the QLM have been deposited on fluvial terraces (Sun et al., 2017a, 2017b). Because fine grained fluvial deposits (e.g., floodplain) and aeolian loess deposits can have similar grain size characteristics, discriminating between these two types of deposits is not straightforward. This is, however, crucial for palaeo-environmental interpretations during hominin occupation, and for pedostratigraphic correlation with the typical loess-palaeosol sequences on the CLP. The fluvial-aeolian transition also marks terrace abandonment and gives insight in the fluvial morphodynamics of the Hanjiang river.

Our study focuses on a fine grained sedimentary sequence on a fluvial terrace in the eastern part of the Hanzhong Basin, near Baoshan (33°12′14.82″N and 107°20′10.35″E) located in the southern part of the Qinling Mountains (Fig. 1B). In the Hanzhong Basin, hominin artefacts are found in fine grained deposits overlying terraces starting from at least 1.2 Ma (Sun et al., 2017b; Xia et al., 2017). The aim of this research is to determine and characterize the transition of the fluvial to aeolian depositional environment in this sequence inferred from field observations, organic matter and carbonate content, grain size and shape analyses, mineral content (mica's) and end-member modelling of the grain size dataset. The fluvial base of the sequence is dated using terrestrial cosmogenic nuclides (TCN) isochron-burial dating, allowing for a chronological correlation to the CLP sequence independent from the pedostratigraphic correlation. Similar sedimentary sequences on different terrace levels, one in the west of the basin and one to the east of our section, are analysed by Yang et al. (2019, Fig. 1B).

2. Geologic and geomorphologic setting

The Qinling Mountains (QLM) have an elevation of about 2000–3000 m above sea level (a.s.l.) and consist of Palaeozoic and Mesozoic rocks that have been uplifted during the Neogene and the Quaternary. The Hanzhong Basin is one of several intramontane basins in the QLM; the Ankang- and Yunxian basins are the most significant other examples (Fig. 1A, Rost, 1994). The uplift of the QLM and the basin formation is an effect of the India-Asia collision (Sun, 2005). The Hanzhong Basin has a general elevation of about 500 m a.s.l. It has a length of ~100 km in a W-E direction and a width of ~50 km in a N-S direction. The Hanjiang River, a tributary of the Yangtze River, drains the southern part of the QLM and flows through the Hanzhong, Ankang, and Yunxian basins. In the Hanzhong Basin, the Hanjiang River has six terrace levels (T1-T6) (Zhang et al., 2013; Sun et al., 2017a, 2017b). A preliminary terrace map, based on our own field observations (correlation of the height of the terrace surfaces and the height of bedload gravel deposits) and analyses of the digital elevation model, shows the distribution of the terrace remnants of T4, T3, T3b, T2a and T2b (Fig. 2). Most of the terraces are preserved on the northern side of the Hanjiang River. The studied Baoshan section is located on a terrace remnant of T3 (Fig. 1B; red circle in Fig. 2). The sites of Yang et al. (2019) are located on terrace T4 and T2 (Fig. 1B). As illustrated by Sun et al. (2017b), the terrace surfaces of T3 and T2 could locally have a significant height difference of up to 33 m in the western part of the basin. The height difference between T3 and T2 at the Baoshan section is ~20 m as shown in the cross profile in Fig. 2. The profile also illustrates that the terrace remnant of T3 is highly dissected by gullies, whereas T2 shows a more flattened surface. Sun et al. (2017b) pedostratigraphically correlated the loess-palaeosol sequence on terrace T3 with S1 to S5 (~0.079–0.625 Ma). The fluvial deposits of T3 are therefore older than 0.625 Ma.

The lithological composition of the fluvial gravel deposits of the six terraces is similar. The gravels are composed of quartzite, vein quartz, quartzitic sandstone, limestone and granite. The terrace deposits have thicknesses varying between ~3–22 m. Their base, ~2–10 m thick, consists of gravels with sand. These are overlain by fluvial sands of ~0.5–7 m in thickness. A cover consists of 20-m-thick layer of fine grained

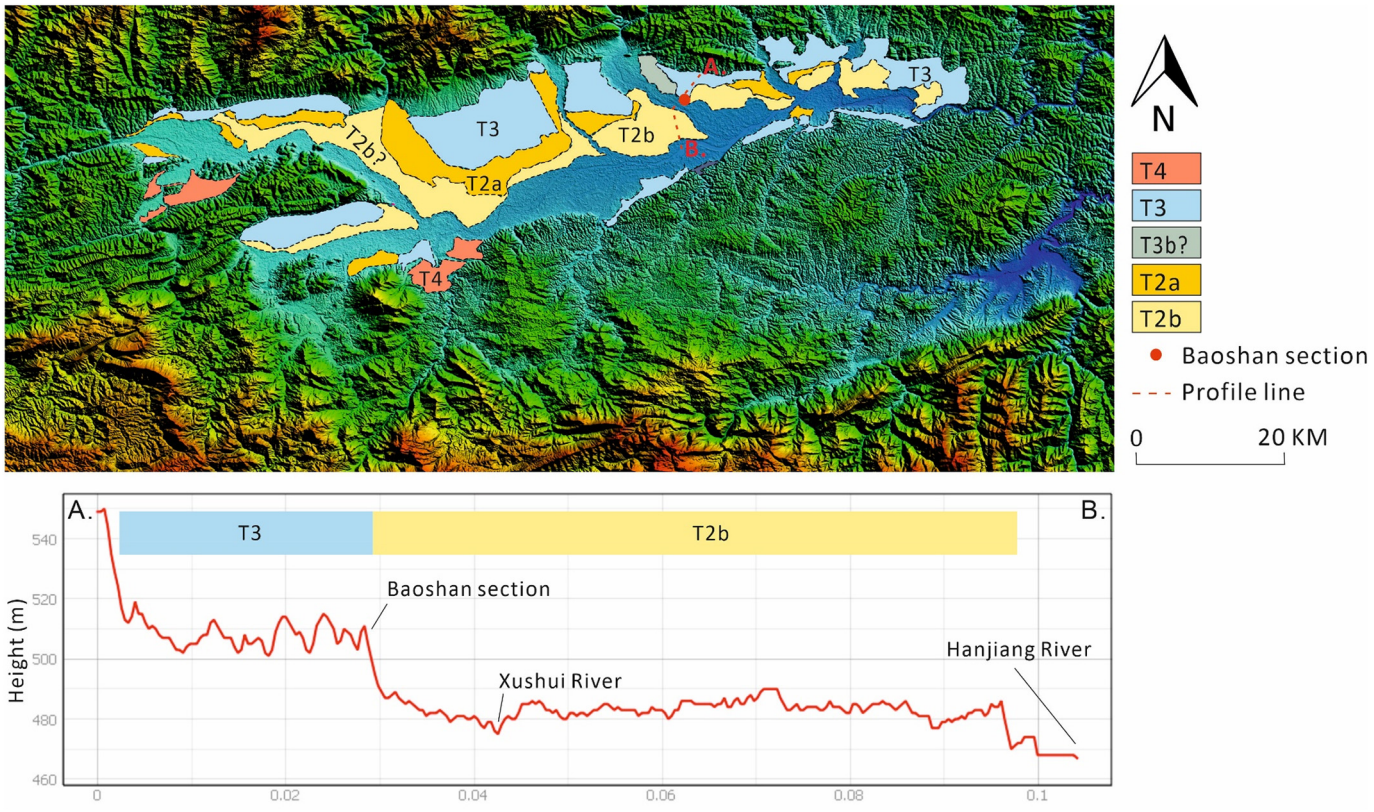

Fig. 2. Preliminary terrace map showing the terrace remnants of T4, T3, T3b?, T2a and T2b in the Hanzhong Basin and a cross profile showing the height of the terrace surface near the Baoshan section.

deposits (clays and silts) over the coarse-grained fluvial deposits (sand and gravel). These clayey silts contain carbonate and ferromanganese concretions, are mottled, with a vertical cleavage and a blocky structure. They are, therefore, interpreted as loess and palaeosol layers (Sun et al., 2017b). These loess deposits have been deposited at lower sedimentation rates, and they are finer grained and more intensely weathered compared to the loess deposits on the Central Loess Plateau (CLP, Zhang et al., 2012; Guo et al., 2013; Sun et al., 2017a, 2017b). Because of these characteristics, these deposits are often referred to as atypical loess (Sun et al., 2017a).

3. Material and methods

3.1. General overview of the Baoshan section

The Baoshan section is composed of seven profiles (A to F, and X, Fig. 3). Profiles A to D and X are located in a clay brick quarry (Fig. 3B, C). Profile A (810 cm in length), B (755 cm) and C (480 cm) are located on the main wall of the brick quarry. Profiles A and B slightly overlap; the top of profile B correlates with a depth of 700 cm in profile A. Profile C is a direct continuation of profile B but with several meters of horizontal offset. Profile X (120 cm) is located opposite of the main quarry wall. Its top correlates with the base of profile C; its base is at the quarry floor. Profile D (240 cm) is located in a pit dug in the quarry floor. Gravels were exposed in a ditch in a lower part of the quarry floor. This part of the quarry could not be sampled, but the height difference between the base of profile D and the top of the gravel unit could be measured. Profiles E and F are located at a cliff exposure, 800 m south of the quarry (Fig. 3D). Profile E (410 cm) overlies profile F of which only the topmost ~300 cm is exposed; it consists of fluvial sand and gravel deposits. The top of profile E is correlated to the base of profile D, based on barometric height measurements and correlation of the top of the gravel deposits. The composite clayey silt sequence (Fig. 4.) consisting of profiles A to E has a total thickness of 27 m and is analysed at 30-cm resolution. Two grain size samples of profile F are taken from different sand layers. Fieldwork and sampling was executed in May–June 2017.

3.2. Organic matter and carbonate analyses

Organic matter and carbonate contents were determined using a *LECO Thermo Gravimetric Analyzer 701* in the Sediment Laboratory at the VU Amsterdam. Thermo gravimetric analysis measures the weight loss (loss on ignition) as a function of temperature from 25 to 1000 °C of 1–2 g of homogenized material. Because of the vaporized water content of the matrix, the first weight loss was at 105 °C. At 330 °C the less resistant organic material was burned; the remaining more resistant organic material was burned at 550 °C. The sum is here reported as total organic matter content. The subsequent heating to 1000 °C resulted in dissociation of carbonates (Konert and Beets, internal VU report).

3.3. Grain size and shape analyses

Laser diffraction (LD) grain size analyses within the 0.15–2000 μm size range were performed with a *Sympatec HELOS KR Laser Diffraction Particle Sizer* in the Sediment Laboratory at VU Amsterdam. The samples were chemically pre-treated in order to remove organic matter and carbonates, following an adjusted procedure of Konert and Vandenberghe (1997). The adjusted procedure is needed because of the presence of ferromanganese nodules that react with H_2O_2 (used to oxidize organic material, Konert and Vandenberghe, 1997). The addition of H_2O_2 is repeated three times. To reduce the effect of coarse nodules on grain size analysis, the samples were wet-sieved over a sieve with a mesh size of 500 μm after the first addition of H_2O_2. Siliciclastic material coarser than 500 μm was present with extremely low abundance and put back in the beaker containing the sample.

Dynamic image grain size and shape analysis was done with a Sympatec Qicpic in the Sediment Laboratory at VU Amsterdam. Grain shape analysis is used to determine transportation processes in aeolian sediments (Shang et al., 2017; Tysmans et al., 2009) or to determine the deposition environment (Tunwal et al., 2018). The Qicpic allows for the analysis of several million particles within the 2–500 μm range with a measurement time of 5 min. Because of the 2 × 2 μm pixel size of the Qicpic camera and the very high clay content, we used a lower grain size limit of 20 μm. This is similar to Tysmans et al. (2009) and Shang et al. (2017), who applied dynamic image analysis with a lower limit of 15 and 16 μm, respectively. In order to remove the <20 μm fraction, 2 g of sediment (chemically pre-treated similar as done prior to the LD analysis) was sieved over a 20 μm sieve prior to analysis.

Qicpic grain shape data are based on the contour (2D image) of particles that have passed the camera. The aspect ratio is defined as the ratio of the minimal to the maximal Feret diameter, which is the distance of two tangents to the contour of the particle. In theory, the aspect ratio ranges from 0 to 1, in practice the range is between 0.14 and 0.76 corresponding to a range in shapes from extremely flat or elongated to almost perfectly symmetrical (Shang et al., 2017).

The Qicpic also determines the number of particles present in predefined size fractions. The pre-treated and sieved sediment (2 g) of every sample was analysed for 5 min in 1.8 L of demineralized water. The parameters were kept constant, hence the particle count of each sample could be compared. The size fractions that were used are >20 μm for the total particle count, >63 μm for the total sand particle count, and >100 and >200 μm for the fine-medium sand fractions. The >100 and >200 μm size fractions were also expressed as relative counts of the total particle counts.

3.4. End-member modelling

Unmixing of grain size data by end-member modelling was used to determine subpopulations in grain size distributions of sediments, which may not be readily visible in distributions of individual samples (e.g. Prins and Weltje, 1999; Weltje and Prins, 2003, 2007). We used the *AnalySize* algorithm (Paterson and Heslop, 2015) to decompose the Baoshan grain size dataset. The dataset consists of multiple grain size distributions (GSDs) (n = 99). In the first modelling step, the number of end-members was determined using the sample-wise and class-wise coefficient of determination (R^2) statistics (e.g., Van Hateren et al., 2017). The second step involved calculation of the end-member compositions and the abundance of end-members per sample. The GSDs and the stratigraphic distribution and relative abundance of the end-members were used to extract information about the dominant sedimentary processes (Weltje and Prins, 2003; Prins et al., 2007, 2009; Shang et al., 2018).

3.5. TCN dating

We applied the isochron-burial dating method (cf. Balco and Rovey, 2008) exploiting terrestrial cosmogenic nuclide (TCN) concentrations in buried alluvial quartz and quartzite cobbles of a confined stratigraphic horizon from the base of profile F. We used cosmogenic nuclides ^{26}Al and ^{10}Be, which are produced in the same mineral quartz (cf. Dunai, 2010). Isochron-burial dating allows for the establishment of a burial age for a set of deeply buried samples that share the same post-burial history. Preconditions are that samples were collected from the same confined horizon, they were located at sufficient depth to be shielded from spallogenic TCN production, and that progressive decay of cosmogenic radionuclide concentrations in the samples was uniform. Buried samples may, however, have experienced different (pre-burial) exposure histories so that inherited TCN concentrations are non-uniform (Erlanger et al., 2012). TCN isochron-burial dating exploits these differences and enables separation of variable TCN inheritance in a group of individual clasts (Balco and Rovey, 2008; Granger, 2014). Variations of

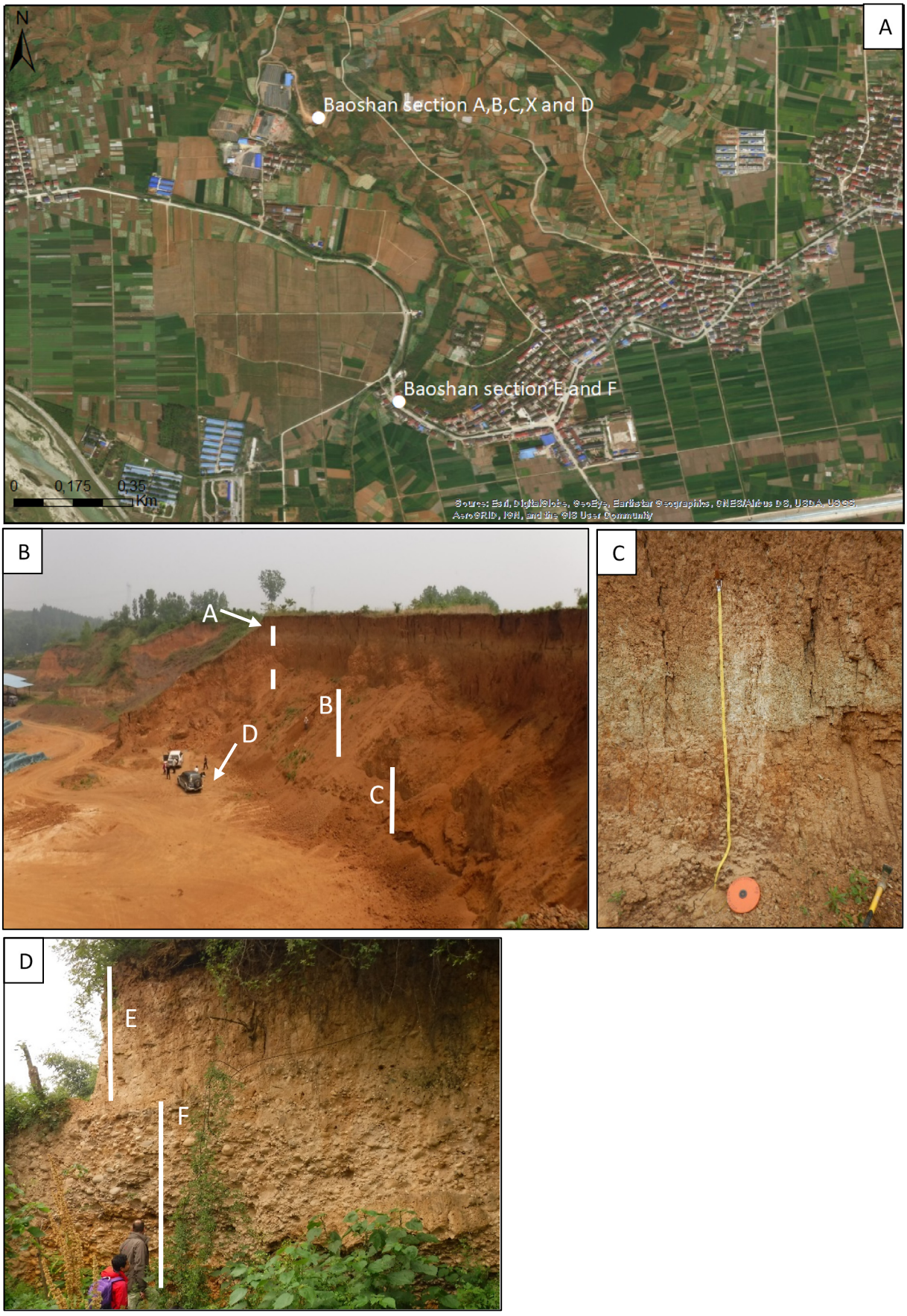

Fig. 3. (A) The location of the profiles (A-F, X) of the Baoshan section. (B) Profiles A to D and X (located opposite of the quarry wall, Fig. 3C) are located in a clay brick quarry. (C) Profile X. (D) Profile E and F located ~800 m south of the quarry.

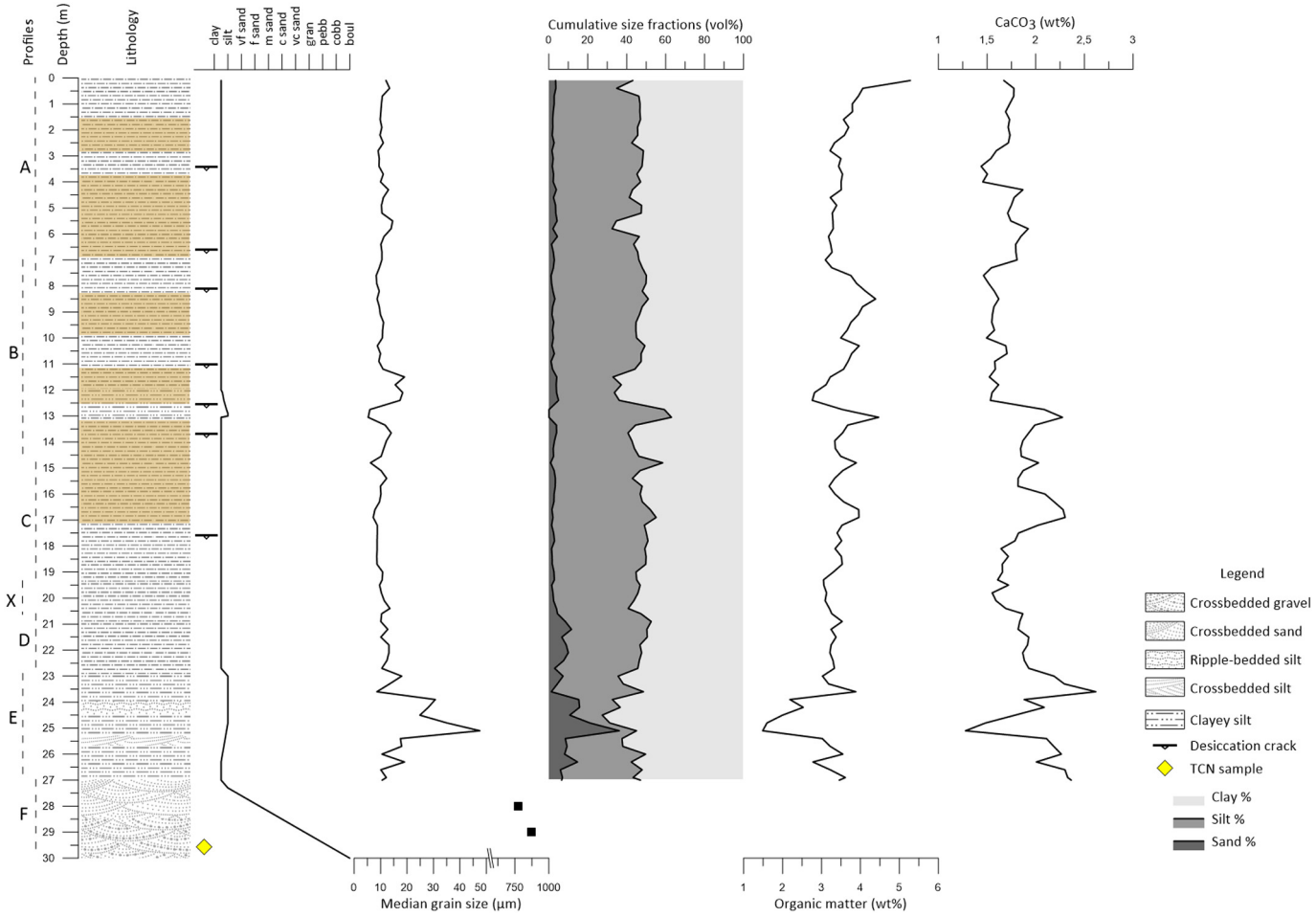

Fig. 4. Composite sedimentary log of the Baoshan section, the profiles are indicated next to the lithostratigraphy as dashed lines. The yellow boxes in the lithology illustrate the characteristic colour in the 7.5 YR range. The sediment composition is shown as median grain size (µm), cumulative clay-silt-sand fractions (vol%), organic matter and calcium carbonate contents (wt%). The parameters illustrate the homogenous characteristics of the top ~23 m of the Baoshan section.

inherited (pre-burial) nuclide concentrations in isochron samples can be used for assessing post-burial (non-spallogenic) TCN production at sample depths of ≥10 m below the surface and for modelling an initial isochron line, i.e., the $^{26}Al/^{10}Be$ ratio at the time of burial (e.g., Akçar et al., 2017). The difference between $^{26}Al/^{10}Be$ surface production ratio at the time of burial and the ratio measured in the buried sediment samples eventually permits the determination of the sediment burial time (Granger, 2006).

Sample processing was done at the CosmoLab of Bremen University. Samples were crushed and sieved to 250–500 µm. To isolate the target mineral quartz, fractions were decarbonized, magnetic minerals were separated, and samples were purified from meteoric ^{10}Be by repeated leaching with 2% HF/HNO_3 at 80 °C. Inductively coupled plasma optical emission spectrometry (ICP-OES) at *MARUM* (Bremen) was used for repeated purity checks, for determining native ^{27}Al content and for estimating the quartz mass required for dissolution. After spiking with a ^{9}Be-standard solution (i.e., 1000 mg/L, *Scharlab*), samples were dissolved in *HF*. Beryllium and Al target elements were isolated and extracted using state-of-the-art single-step column chromatography (Binnie et al., 2015). Following calcination, target cathodes were prepared for $^{10}Be/^{9}Be$ and $^{26}Al/^{27}Al$ isotope measurements at *CologneAMS*. The $^{10}Be/^{9}Be$ and $^{26}Al/^{27}Al$ measurements were normalised to the standards of Nishiizumi et al. (2007, 2004), applying KN01-6-2, KN01-5-3, and KN01-4-3 standards. Systematic errors and analytical uncertainties (e.g., AMS counting, standard scatter, etc.) were factored into the reported age uncertainties.

4. Results

4.1. Lithostratigraphy

Fig. 4 illustrates the composite sedimentary log of the Baoshan section and Fig. 5 provides photographs. The basal part of the section (30–27 m, Fig. 5C, D) consists of gravel and sand layers (profile F). Imbrication of the gravels indicates a flow direction towards the south. The gravels are mainly composed of sub-rounded to rounded quartzite, vein quartz, quartz sandstone, limestone and granite.

The interval from 27 to 23 m consists of fine grained fluvial deposits composed of very fine sand and silt (Fig. 5B). Cross-bedded sandy intervals of ~5 cm thick, horizontally laminated sand and silt beds of 1–2 mm (Fig. 5G) and sand-sized micas (muscovite) mixed with silt-sized grains indicate a low energy fluvial origin. We found a strong colour variation in this interval, ranging from yellow (10YR 7/6) to reddish yellow (7.5YR 7/6). At the base of the interval, the colours show moderate to heavy mottling. Iron- and manganese-oxide precipitates (black spots) are present. Black ferromanganese nodules of 1–10 mm in size are present in varying abundance in the 24–23 m interval (Fig. 5E).

In general, the remaining 23 m long part of the composite section (Fig. 5A) consists of strongly weathered homogenous clayey silts with characteristic colour changes (10YR to 7.5 YR). The interval ranging from 23 to 20.6 m deep consists of homogenous silt with an overall very pale brown colour (10 YR 7/4), and shows mottling with pink/reddish yellow colours (7.5 YR 7/4–7/6). Black ferromanganese nodules are very low in abundance in the 23–21.5 m interval; the nodules increase

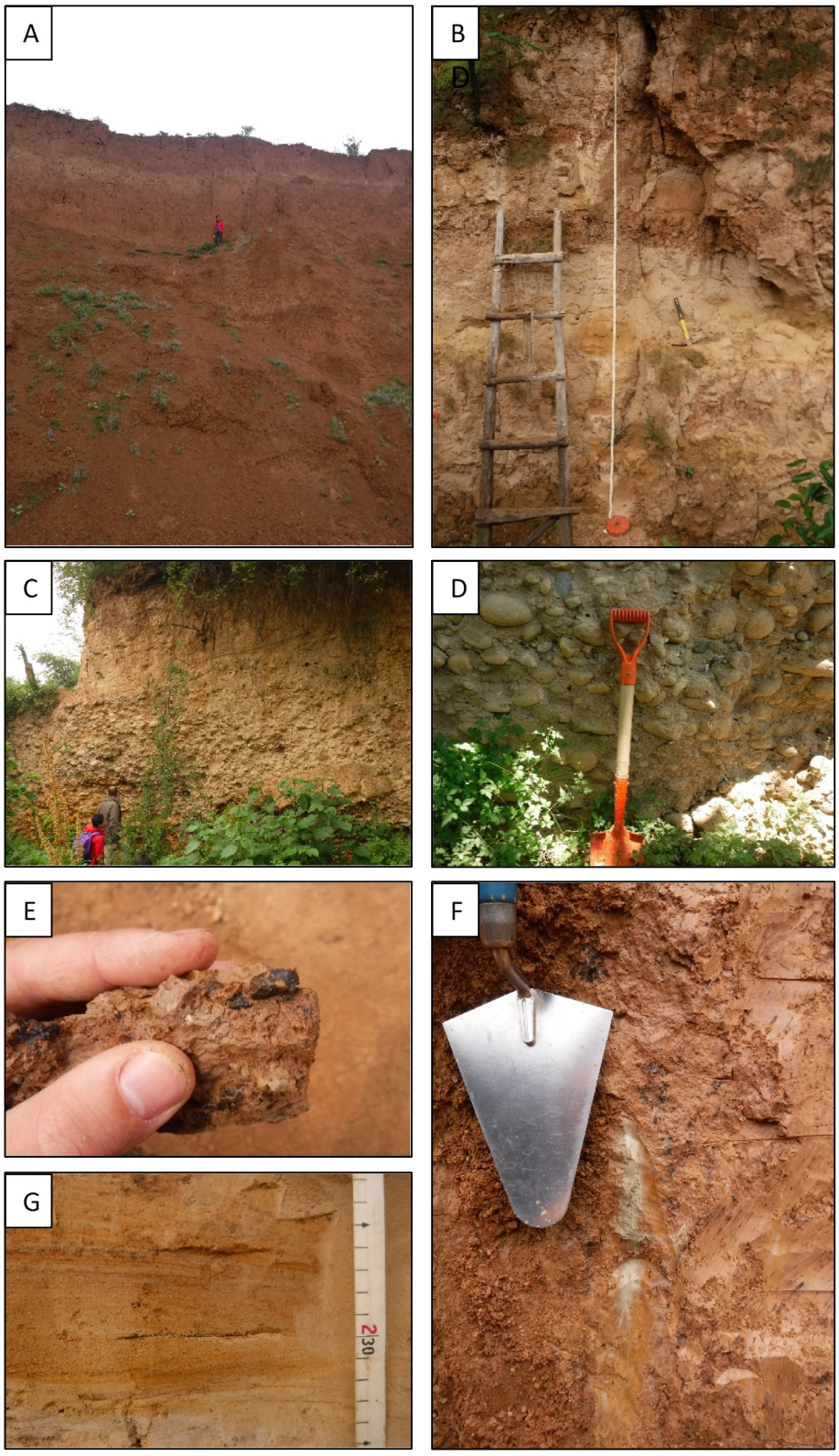

Fig. 5. (A) Clayey silt deposits of the top ~20 m in profiles A, B and C. (B) Overview of profile E. (C) Overview of profile F and E. (D) Gravels of profile F. (E) Example of nodules present in the clayey silt deposits. (F) Example of grey vertical structure present in the loessic deposits. (G) Horizontal- and cross-bedding in profile E.

in abundance towards the top of the interval at 20.6 m. Micas are present, but they are less abundant compared to the interval at 27–23 m. At a depth range of 20.6 to 17.2 m, the section is composed of clayey silt with a pale brown colour (10 YR 7/4) and shows mottling with light brown (7.5YR 6/4) patches. From 20.2 to 19.8 m depth, the colour changes to light grey (2.5Y 7/2). The interval has a low abundance of nodules. The nodules vary in size (2–15 mm), and sometimes they have a branched appearance. Two meters away from the sampled section, at a depth of 19.8–19.4 m, a poorly-sorted mixture of clay, silt, sub-angular sand and angular pebbles is present. From ~17.2–13.2 m

depth, the overall colour changes to 7.5YR 6/4. The degree of mottling varies at a dm-scale from none to strong. From 15.3–14.5 m depth, the colour changes to pink-reddish yellow (7.5YR 7/4–6/6), the base of this part is strongly mottled. The abundance (low to extremely high) and size (1–15 mm) of ferromanganese nodules varies with depth, but shows a general decrease towards the top of the layer. Pinkish grey (7.5YR 7/2) vertical structures (Fig. 5F) are present throughout this interval. The structures vary in size between 2 and 30 cm in length and 1–2 cm in width. A few angular quartzite grains and flakes (2–7 mm) of unknown origin are present at various stratigraphic levels (16.16, 16.14, 15.72, 15.46, 15.30, 15.15, 15 and 14.75 m). The interval from 13.2–6.9 m consists of homogenous clayey silt but can be subdivided into five layers based on colour. The size (up to 1 cm) and abundance (low to very high) of ferromanganese nodules vary with depth. Grey vertical structures are present throughout the section and are variable in size (1–5 cm length and 1–2 cm width). The first layer, from ~13.2 to 12.5 m, has a very pale brown colour (10 YR 7/4). The second layer (12.5–11.25 m) has a reddish yellow colour (7.5YR 7/6). The third layer (11.25–9.85 m) has a very pale brown to (10YR 7/4) yellow colour (10YR 7/6). The fourth layer (9.85–8.45 m) is reddish yellow (7.6 YR 6/6). The fifth layer (8.45–6.9 m) is very pale brown (10YR 7/4). Sediments of the top 6.9 m consist of clayey silt. From 6.85 to 3.80 m depth, a reddish yellow (7.5YR 6/6) layer occurs, with a high abundance of ferromanganese nodules and grey branched vertical structures of 1–5 mm in width. The colour gradually changes to very pale brown (10YR 7/4) in the layer present at 3.80–2.30 m depth. The base of this layer has abundant nodules and branched grey vertical structures; both characteristics are absent at the top of the layer. The next layer is a pink (7.5YR 7/4) layer of 1.2 m in thickness (depth range 2.80–1.60 m) with a sharp upper and lower boundary. It has a low abundance of nodules. The uppermost 1.6 m has a very pale brown (10YR 7/4) to light brown colour (7.5YR 6/4) and has a very low abundance of nodules.

4.2. Sediment composition based on laser diffraction and thermal gravimetric analysis

The median grain size, the clay, silt and sand content, and the total organic matter and carbonate contents for the upper 27 m of the composite section are plotted next to the sedimentary log in Fig. 4. The median grain size of 10–15 μm clearly illustrates the homogenous character of the section. Only the interval 26–24 m in depth shows slightly coarser grain size values, with a median grain size up to 48 μm. The two sandy samples of profile F (27–30 m) have a median grain size of 775 and 865 μm. At 27–25 m, the sand content is below 10 vol%. From 20.5 to 25 m in depth, the sand content increases to about 36 vol%. In the upper 20.5 m of the section, the percentage of sand is more or less constant and does not exceed 5 vol%. The amount of silt varies between 37 and 72 vol%; the average is 54 vol%. The clay content varies between 30 and 60 vol%, with an average of 42 vol%. In the sandiest part of the section, around 25 m, the contribution of clay varies between 9 and 20 vol%; in the basal part it is 40 vol%. The grain size characteristics clearly demonstrate that the section is mainly composed of clayey silt.

Average grain size distributions (GSDs) of each of the Baoshan profiles are shown in Fig. 6. Profiles A to X have similar distributions, with a modal size of ~25 μm. Profile D has a similar distribution and mode but with a slight increase in the >100 μm fraction. GSD's of these profiles show two shoulders at 2 μm and 10 μm. Profile E illustrates a more unimodal distribution, with a modal size of 32–35 μm and increased >100 μm fraction. The latter increase is primarily the result of the presence of (sand-sized) mica particles. The samples of profile F consists of very coarse sand with a mode of ~1000 μm. This interval also contains a few percent of gravel.

The total organic matter and carbonate contents show very low values throughout the composite section (Fig. 4), on average 3.4 and 1.8 wt%, respectively. It is important to note that the values are close

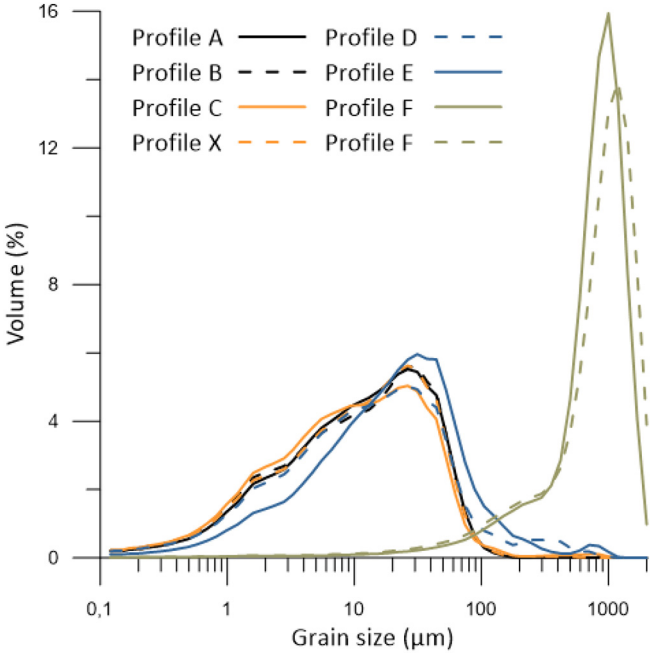

Fig. 6. Average grain size distributions (within the 0.15–2000 μm size range) of profiles A-E and X, and the grain size distributions of the two samples of profile F.

to the detection limit of the thermo gravimetric analysis instrument. Moreover, the correlation between the grain size composition (mainly clay content) and the organic matter and carbonate results illustrates that the latter values are most likely strongly affected by the high clay content. This can be explained by clay minerals losing their bonded hydroxyl groups as water at different temperature ranges while heating from 105 °C to 1000 °C (in addition to decomposition of organic matter and carbonates; Konert and Beets, Internal VU report). Next to the (unknown) clay mineral type and abundance, the observed ferro-manganese oxides also might have affected the reported organic matter and carbonate results.

4.3. End-member modelling

Fig. 7 shows the end-member modelling statistics for mixing models using two to ten end-members. The sample-wise R^2 is high for all number of end-members, but shows a clear inflection point at the model with four end-members. The average class-wise R^2 indicates high values of 0.8 or more, starting from a model with four end-members (Fig. 7B). The two and three end-member models show very low R^2 values within the 10–30 μm and >100 μm grain size range. The four to ten end-member models illustrate notably high R^2 up to 300 μm. Only the nine and ten end-member model illustrate high R^2 within the whole grain size range. Based on the class-wise R^2 data, both a four (Fig. 8) and five end-member (Fig. 9) model represent a mixing model that adequately describes the grain size dataset.

The most significant difference between the four and five end-member model is in the composition and distributions of the coarse end-members (EM4 of the 4 end-member model, and EM4 and EM5 of the five end-member model). For both models, the coarsest end-member is composed of a bimodal distribution with modes of ~53 and ~200 μm. In the four end-member model, the coarsest end-member is dominant in the basal ~7 m (profile E, D and partially X) but it also has significant (up to 7%) abundances in several layers, higher in the composite section. In the five end-member model, the coarsest end-member is present almost exclusively in the lower part of the composite section. This is also the part of the section where the sand-sized micas occur, explaining the coarse mode. The presence of sand size micas mixed with silt is only observed in the fluvial part of the sequence (profile E).

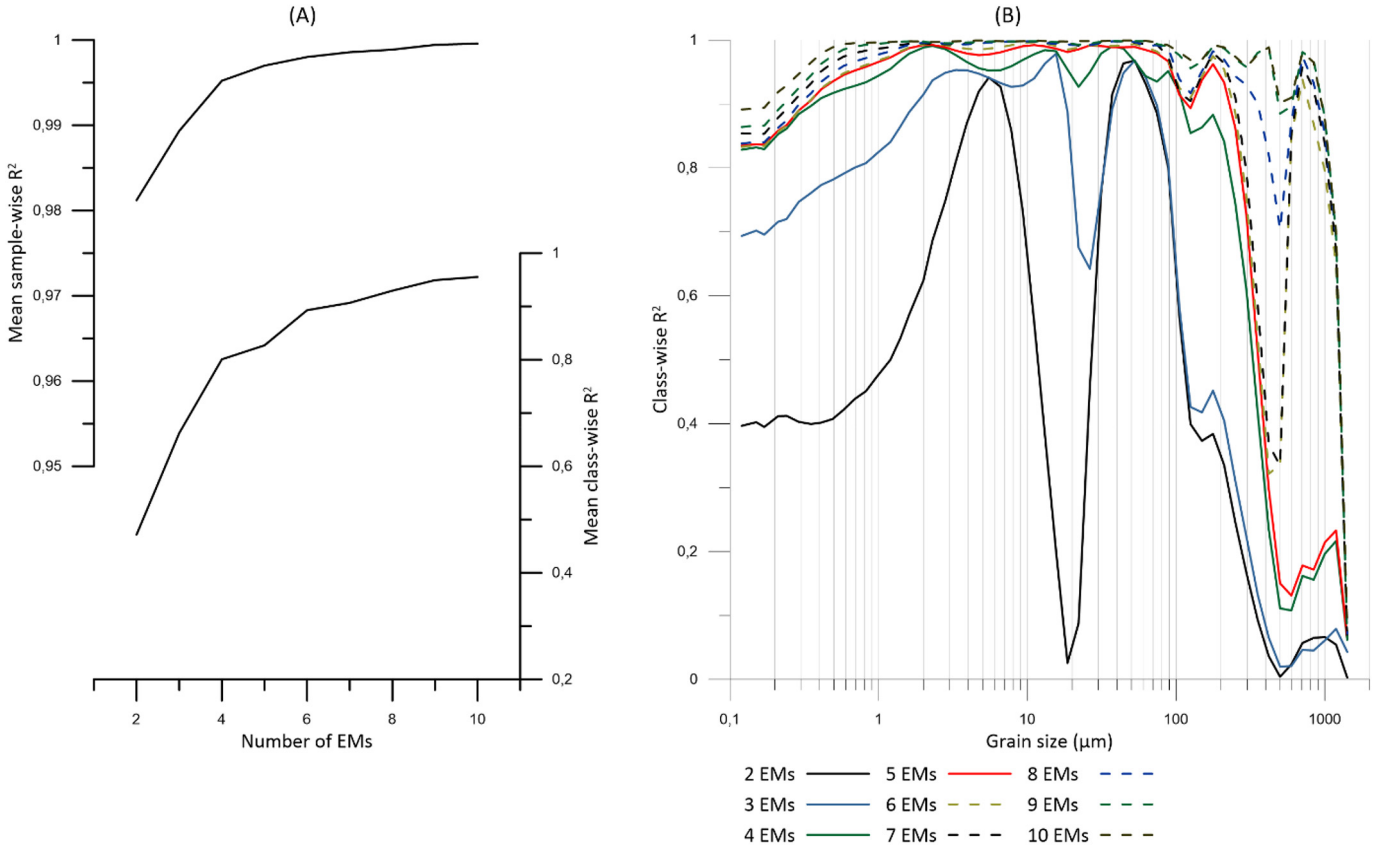

Fig. 7. End-member modelling statistics of the grain size data set. (A) The mean sample-wise and mean class-wise coefficient-of-determination (R^2) as a function of the number of end members (EMs). (B) Class-wise R^2 for each size class for 2 to 10 end-member models.

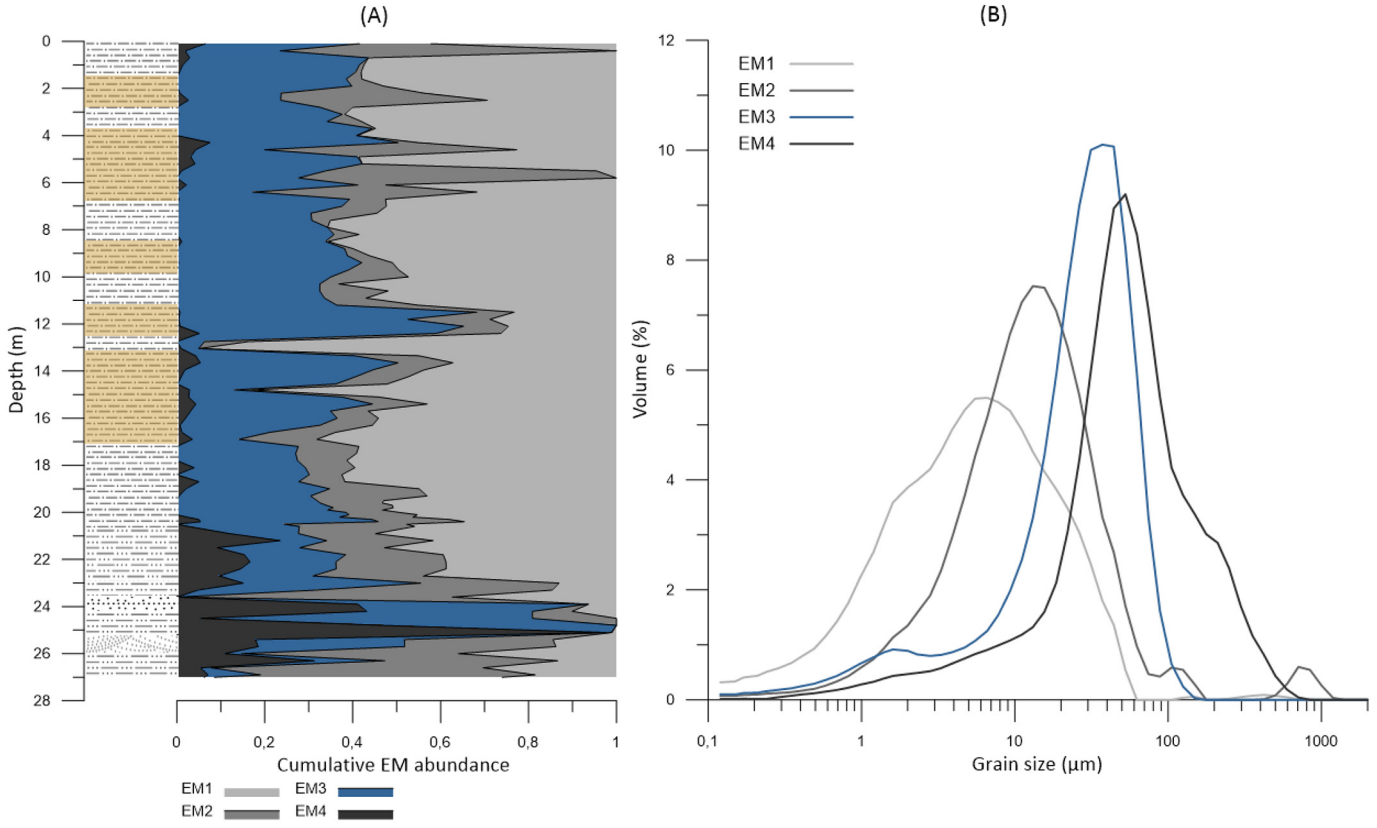

Fig. 8. The end-member modelling results for the 4 end-member model. (A) Cumulative end-member abundance plotted next to the lithostratigraphic column. (B) Modelled end-members with a modal grain size of ~6 µm (EM1), ~14 µm (EM2), ~37 µm (EM3) and ~52 µm (EM4).

Therefore, the five end-member model is chosen as it appears to provide a better unmixing solution.

Fig. 9 shows the results for the five end-member model, depicting the end-member abundances with depth (Fig. 9A) and the grain size distributions of the end-members (Fig. 9B), respectively. EM1 is the finest end-member, with a mode of 6 μm and a maximum grain size of 50 μm. EM2 has a mode of 14 μm and a maximum grain size of 74 μm. EM3 has a modal size of 31 μm with a maximum size of ~150 μm. EM4 has a mode of 44 μm and a maximum size of 150 μm. EM5 is the coarsest end-member and has a bimodal distribution, with a modal size of 53 μm and a second mode of ~200 μm, with a maximum grain size of ~800 μm.

The average abundance for each end-member for the whole composite section (Fig. 9A) is 0.34 for EM1, 0.22 for EM2, 0.27 for EM3, 0.12 for EM4 and 0.05 for EM5. In the lowermost 3 m (27–24 m) there is an alternation of pulses of coarse (EM4 and EM5) and fine end-members (EM1-EM3). EM4 and EM5 are dominant between 25 and 24 m depth and sharply decrease to ~4% at 24 to 23.5 m. From 24 to 21 m depth, EM5 and EM4 are present but less abundant compared to the basal part. At a depth of 21 m, EM5 decreases to negligible amounts, except for some minor increases to a few percent. From about 20 to 17 m depth, the end-members illustrate a homogeneous composition with EM1, EM2 and EM3 being the most dominant, with one increase in abundance of EM4 around 19 m depth. In the interval at 17–13 m depth, the abundance of EM4 increases. The intervals at ~14, 12, 9 and 5 m show similar characteristics of increased abundance of EM4.

4.4. Particle counts and grain shape based on dynamic image analysis

Plotted next to end-member abundances of the five end-member model are the particles counts for particles >20, >63, >100 and >200 μm (Fig. 10). For particles >20 μm, a minimum of ~80 × 10^3 and a maximum number of ~471 × 10^3 have been counted per sample. The highest counts, with an average value of ~326 × 10^3, occur in profile E (up to ~23 m depth). The counts decrease to an average amount of ~153 × 10^3 in profile D (~21 m depth). The upper ~21 m have an average particle count of ~139 × 10^3, but locally excursions up to a maximum of ~383 × 10^3 counts occur. The particle counts show a strong correlation with the end-member abundances.

The particle count for the sand fraction (>63 μm) shows significantly lower values compared to the total particle count. The lower 4 m of the section have the highest contribution of sand, with an average particle count of 4.5 × 10^3 and a maximum count of 9.9 × 10^3. The upper 23 m has an average of1.2 × 10^3 particles, with some minor excursions. The particle count for the >100 μm fraction shows a similar trend, but with significantly lower values (maximum count = 88) The contribution of grains >200 μm is very low (maximum count = 10) and does not significantly contribute to the total particle counts. The relative abundances of the >63 μm and >100 μm sand fractions, expressed in per mil (‰) with respect to the total >20 μm fraction, are plotted in Fig. 10D. Both graphs illustrate the low contribution of sand compared to the total particle count.

Grain shape characteristics of each profile is shown in Fig. 11 The graph shows a decreasing aspect ratio with increasing grain size, indicating less symmetrical grains (increased elongation or flatness) with increasing grain size. Profiles A to X show very similar shape distributions, although the particles >75 μm in profile A show some deviant aspect ratio values. Profile E shows significantly lower aspect ratio values over the whole grain size range in comparison with the other profiles.

4.5. Isochron-burial age calculations

Five quartz-bearing cobbles were collected from the same depth interval of the gravel deposits in profile F, along an isochron-window located at 10 m (±50 cm) below the transition from coarse (sand) to fine grained (silt and clay) deposits (Table 1). The massive quartzite

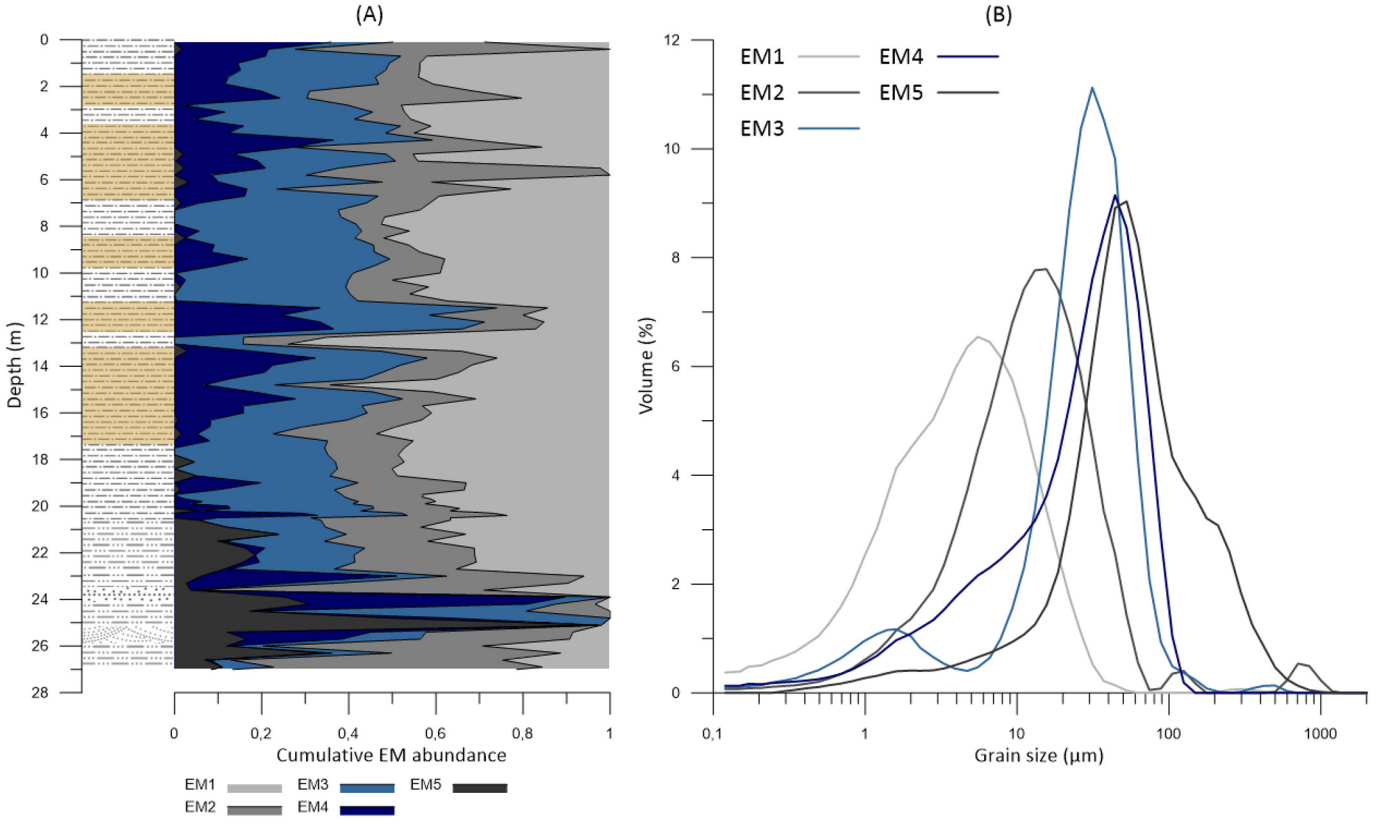

Fig. 9. The end-member modelling results for the 5 end-member model. (A) Cumulative end-member abundance plotted next to the lithostratigraphic column. (B) Modelled end-members with modal grain size of ~6 μm (EM1), ~14 μm (EM2), ~37 μm (EM3), ~44 μm (EM4) and 53 μm (EM5).

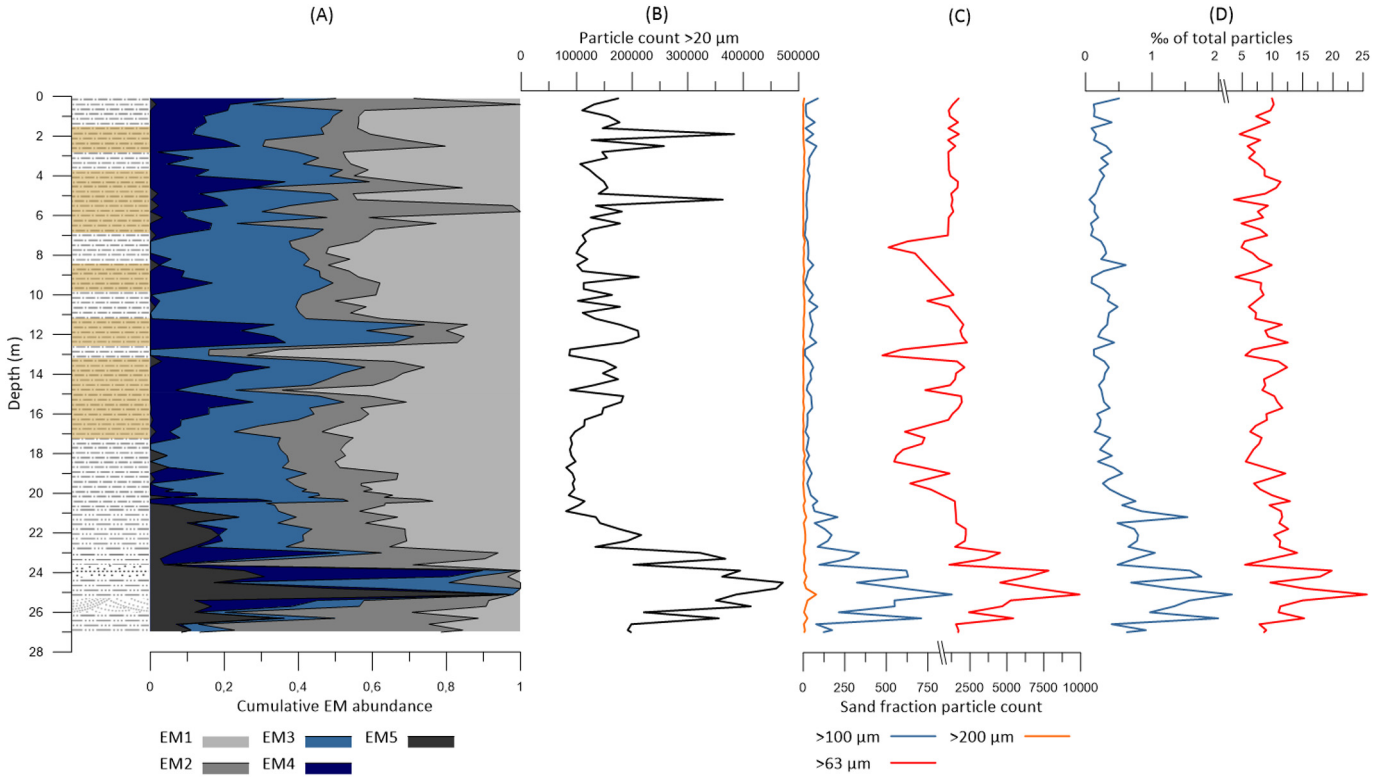

Fig. 10. (A) Cumulative end member abundance for the 5 end-member model plotted next to the lithostratigraphic column. (B) Total particle count (>20 µm) as determined by dynamic image analysis. (C) Particle count for three sand fractions, >63 µm, >100 µm, and >200 µm. (D) Relative particle counts for the >63 µm and >100 µm fractions, expressed in ‰ of the total particle count.

cobbles (~2.65 g cm^{-3}, >1.4 kg) were hardly weathered, only showing smooth oxidized surfaces with <1 mm weathering cortices.

For assessing potential scatter in the dataset and whether samples underwent simple or complex exposure-burial histories, ^{26}Al/^{10}Be ratios were plotted against the measured ^{10}Be concentrations using the CosmoCalc tool by Pieter Vermeesch (http://cosmocalc.googlepages.com). Applying the scaling scheme of Lal with a factor of 1.3, the resulting "banana plot" (Lal, 1991, Fig. 12) shows that all samples plot beneath the steady-state/zero-erosion lines (black) and therefore underwent complex exposure-burial histories. With regard to the calculated ^{26}Al/^{10}Be nuclide ratios, two groups of samples can be distinguished of which subset A (i.e., samples X1 and X4) have significantly lower values. Because radio-nuclide ^{26}Al decays approximately twice as fast as ^{10}Be (e.g., Dunai, 2010), this indicates that these two samples share a much longer (or multiple) burial history.

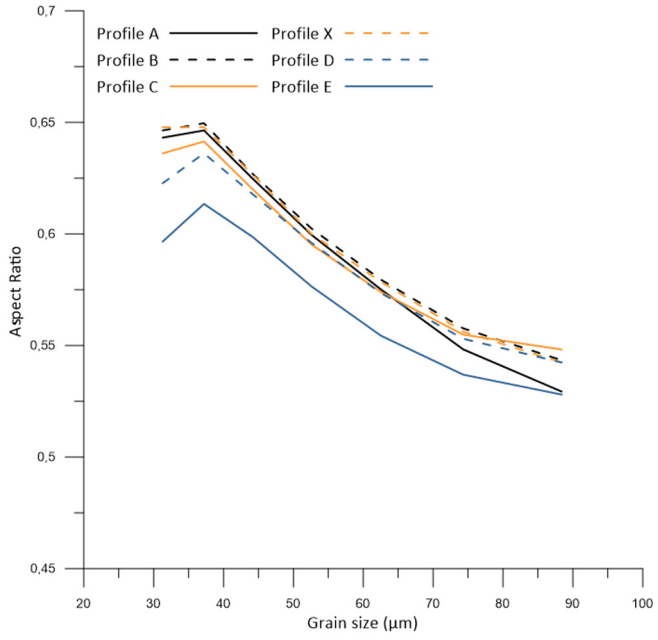

Fig. 11. Average grain shape distributions for profiles A-E and X. The graphs show a decreasing aspect ratio, illustrating increased flatness and/or elongation with increasing grain size.

In a second step, the measured ^{26}Al concentrations were plotted against the measured ^{10}Be concentrations and a linear regression was fitted through the data points (Fig. 13). Initial burial age estimates for the data (sub) sets were then calculated from the slope (R) of the isochron regression lines following:

$$T_{burial} = -\ln \frac{\frac{R}{R_b}}{\lambda_{26} - \lambda_{10}} \quad (1)$$

where R_i is the slope of the initial isochron at the time of burial, and λ are the decay constants of cosmogenic ^{10}Be and ^{26}Al, respectively. Applying standard mean lives of 1.02 Ma (^{26}Al) and 2.005 Ma (^{10}Be) and an initial ^{26}Al/^{10}Be surface production ratio of 6.75 (Balco et al., 2008), calculations yielded the following burial age estimates: 3.274 Ma for subset A; 0.609 Ma for subset B (i.e., X2 + X3 + X5); and 0.639 Ma (full dataset). Taking into account that initial erosion rates were high (cf. Fig. 12), the correction for the initial ratio at the time of burial is at most 2%. As shown in Fig. 12, preliminary age estimates denote two different sample populations of which subset A contains apparent outliers and subset B is more reliable with regard to the burial age estimate obtained for the full dataset.

In the last step, isochron-burial ages were calculated following the calculation steps of Granger (2014). Using the MATLAB® script provided by the author (personal communication, 2018), burial ages were computed for the dataset and for subset B using a regression

Table 1
Sample data and AMS results for ^{26}Al and ^{10}Be isotope measurements.

Sample ID	Sample type	Quartz mass dissolved (g)	^{9}Be carrier mass (g)	^{10}Be/^{9}Be ratio	^{10}Be/^{9}Be 1σ	^{10}Be conc (at/g)	^{10}Be uncert. (at/g)	^{26}Al/^{27}Al	^{26}Al/^{27}Al 1σ	^{27}Al conc. (at/g)	^{26}Al conc. (at/g)	^{26}Al/^{10}Be ratio
X_1	Cobble	20.193	3.065E−04	7.86E−14	3.70E−15	7.788E+04	5752	7.947E−14	9.670E−15	2.303E+18	1.830E+05	2.35
X_2	Cobble	10.454	3.069E−04	8.87E−14	4.63E−15	1.704E+05	4587	1.700E−13	1.240E−14	4.934E+18	8.388E+05	4.92
X_3	Cobble	12.630	3.285E−04	2.76E−14	1.92E−15	4.503E+04	6300	6.102E−14	7.790E−15	2.861E+18	1.746E+05	3.88
X_4	Cobble	20.045	3.103E−04	9.21E−14	3.99E−15	9.341E+04	8102	9.931E−14	1.160E−14	2.415E+18	2.398E+05	2.57
X_5	Cobble	10.271	3.056E−04	1.89E−14	1.48E−15	3.396E+04	9221	3.282E−14	5.480E−15	5.552E+18	1.822E+05	5.37

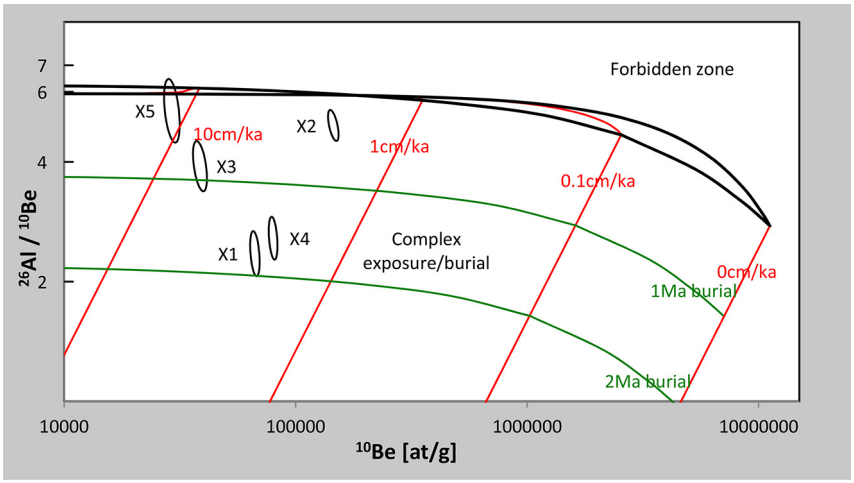

Fig. 12. Banana plot overview produced with CosmoCalc by P. Vermeesch showing the analytical results for the TCN burial data set of five quartz-bearing cobbles.

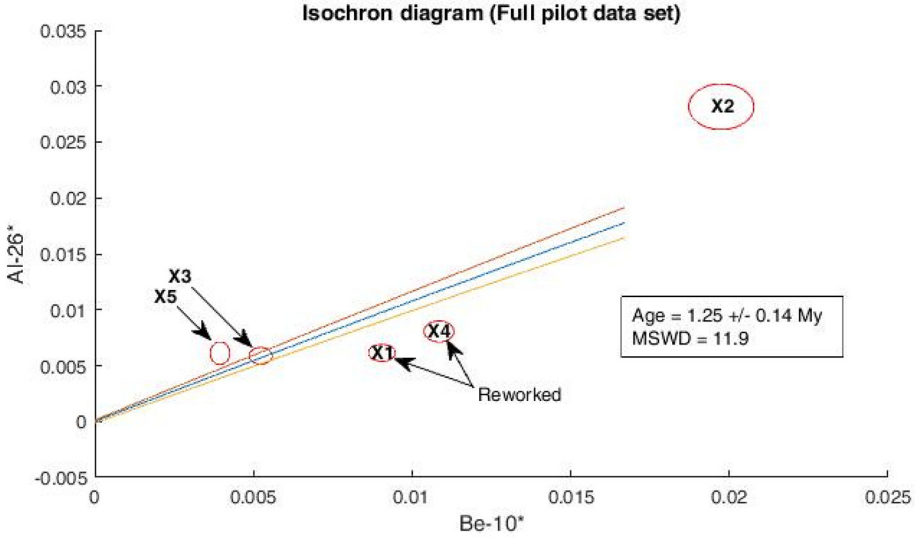

Fig. 13. Isochron-burial diagram showing all data points as error ellipses (i.e. linearized data) and the isochron line of the full data set (blue), and the upper (red) and lower (yellow) 1 sigma solution space (MATLAB script provided by Darryl Granger).

method (York et al., 2004) that accounts for uncertainties in both ^{10}Be and ^{26}Al (cf. Table 1).

As expected, the full dataset produced a much older burial age with unacceptably high mean square weighted deviation (MSWD, Fig. 13). This confirms that samples X1 and X4 are probably reworked and share a previous (potentially repeated) burial history. Samples X1 and X4 are thus regarded outliers and were excluded from the final fit. Fig. 14 shows the results for Subset B, excluding outliers. The calculated isochron-burial age for the Hanjiang River terrace gravel was calculated at 0.60 ± 0.14 Ma, based on the remaining three sample dataset.

5. Discussion

5.1. Fluvial or aeolian?

The Baoshan section consists of at least 7 m of fluvial deposits at the base (30–23 m), which are overlain by ~23 m of clayey silt deposits. The base of the fluvial deposits consists of a fining-up sequence of gravel and sand (3 m thick) with silty deposits on top (4 m thick). The median grain size of the silty deposits varies between 45 and 10 μm. The silty sediments contain a significant proportion of sand-sized micas. The overlying deposits have very homogenous grain size characteristics.

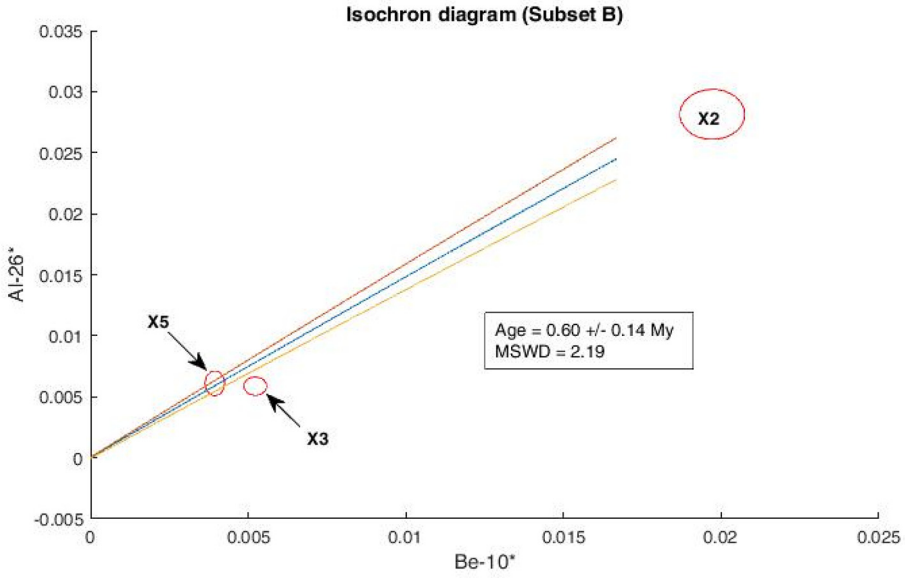

Fig. 14. Isochron-burial diagram of the data subset B (excluding outliers X1 and X4) showing subset data points as error ellipses (i.e. linearized data), the burial isochron line (blue), the upper (red) and lower (yellow) 1 sigma solution space.

The sediments consist of silt and clay with a median grain size varying between 10 and 15 μm. Mottling, grey vertical structures (interpreted as desiccation cracks), abundant black ferromanganese nodules and a distinctive colour variation (10YR to 7.5 YR) occur in this part of the section. These characteristics point to strong post-depositional pedogenic processes. The organic matter and carbonate contents are both very low and mirror the subtle grain size variations. Therefore, the compositional changes as determined by the TGA are likely mainly related to dewatering effects caused by the decomposition of clay minerals and by the decomposition of metal oxides (Konert and Beets, Internal VU report). From this, it can be concluded that the organic matter and carbonate contents are both negligible.

The ~23 m thick clayey silt deposits (Figs. 4 and 6) have a modal grain size of ~25 μm. The amount of sand in these deposits ranges between 11 and 0 vol%, with an average of 3 vol%. The highest amount of sand is present in the interval between ~22 and ~21 m deep. The sand mainly consists of micas and only few quartz grains occur. This is similar to the sand deposits in the depth interval of 25 to 23 m, which are definitely of fluvial origin as evidenced by the cross-bedding and horizontal laminations. This interval has a modal grain size of ~32 μm, and it has a higher sand content, between 36 and 1 vol%, with an average of 12 vol%. We therefore conclude that the interval between 23 and 21 m (profile D) is also of fluvial origin.

The characteristics of the remaining 20.5 m of the Baoshan section are similar to other clayey silt-dominated sequences overlying fluvial terrace deposits in the Hanzhong, Ankang, Yunxian, Lushi- and Luonan basins. These deposits are thus far interpreted as aeolian deposits, comprising loess-palaeosol sequences (Lu et al., 2011a, 2011b; Zhang et al., 2012; Sun et al., 2012, 2013, 2014, 2015, 2017b; Fang et al., 2017; Yang et al., 2019).

Also in the Sichuan Basin, located 400 km southwest of the Hanzhong Basin, similar clayey silt-dominated deposits are found, referred to as the Chengdu Clay deposits. These fine grained deposits occur in widely distributed patches on river terraces, alluvial fans and higher land surfaces (Yang et al., 2010). Their formation is still debated, but recent work favours an aeolian origin (Feng et al., 2014; Feng et al., 2016). The Chengdu Clay consists of silt and clay with a modal grain size of ~20 μm mixed with a small amount of sand (modal grain size 150–200 μm). Grey and ferromanganese mottling, calcareous- and ferromanganese nodules and colours similar to those occurring in the Hanzhong clayey silt deposits are the dominant characteristics for these sediments. At the base, sandy silt deposits directly overlying fluvial terrace gravels also illustrate similar characteristics, and they also contain occasional flaky micas. Based on a number of parameters, including grain size characteristics, magnetic susceptibility, quartz content and provenance data (e.g., quartz oxygen isotope values, major- and trace elemental concentrations), Feng et al. (2016) conclude that the Chengdu Clays are of local aeolian origin.

However, in general, the combination of iron-, aluminium- and manganese nodules, mottling, desiccation cracks and fine grain size composition are also characteristics that can be ascribed to floodplain and backswamp deposits (Aslan and Autin, 1998; Kraus, 2002). Backswamp soils are formed in conditions with a changing seasonal water table. Alternating episodes of dry and wet seasons result in shrink and swell processes, resulting in slickenslides, gleyic phenomena and desiccation cracks. This can be attributed to a changing water table and/or poor drainage of the soil due to a high clay content (Kraus, 2002).

Because of the abovementioned reasoning, it is not possible to determine the depositional environment in which the clayey silt deposits of the Baoshan section have formed and, consequently, a possible transition from a fluvial to an aeolian environment, using merely the field observations and the general grain size characteristics. Nonetheless, the homogenous grain size in the upper 20.5 m of the Baoshan section is not in agreement with a fluvial origin. Fluvial fine grained deposits, formed on floodplains, should show much more grain size variation caused by fluctuations in peak discharges (flooding events), and changing proximity to a channel (associated with internal fluvial dynamics, He and Walling, 1998). A second issue contradicting a fluvial origin is the absence of other fluvial deposits within the clayey silt sequence, like channel, bar or levee deposits. A third issue is that the sequence is rather thick. If the 20.5 m of sediment would be a stack of floodplain sediments, remnants of river channel deposits at almost the same vertical position (a few meters lower) should be found somewhere near the studied section. Such deposits have, however, not been encountered.

5.2. Interpretation of the end-member mixing model

The grain size distributions of the end-members are in the silt range, with EM1 the finest grained (modal size ~6 μm) and EM5 the coarsest (modal size ~53 μm). EM5 has a bimodal distribution with modes at ~53 and ~200 μm. EM5 has a high abundance in the lower 6.5 m of the composite section, and it is almost absent in the upper 20.5 m (Fig. 9).

EM5 represents the fluvial sandy silts with abundant sand-sized mica particles. The end-member modelling results confirm the fluvial origin of profile D (23–20.5 m depth), and they indicate a transition from a fluvial to an aeolian depositional environment at 20.5 m in depth. In the 20.5 m thick loess-palaeosol sequence the abundance of EM1, EM2 and EM3 are fairly constant with an average of 0.39, 0.19 and 0.30, respectively. The most significant change in abundance is present in the palaeosol layers and top 3 m of the section, where the abundance of EM4, with a modal grain size of 44 μm, increases to a maximum of 0.37. Following the classification of Vandenberghe (2013), EM3 and EM4 could represent aeolian transport from a proximal source (e.g., floodplains and older terrace levels) and EM2 and EM1 transport in high suspension clouds from a distal source (acting as a background sedimentation). However, in-situ pedogenic clay mineral formation could possibly contribute to the high percentage of clay (Bronger et al., 1998) and therefore abundance of EM1. The two minor modes of 150 and 800 μm in EM2 could suggest admixture of coarser components or, more likely, they represent false secondary modes inherent to the end-member modelling technique (Prins and Weltje, 1999b; Van Hateren et al., 2017). Following the interpretation of Vandenberghe (2013), the end-member abundances reflects a fairly constant background sedimentation (abundance of EM2 and possibly EM1) admixed with an input of a proximal component (abundance of EM3 and EM4). EM3 has a rather constant average abundance of 0.30. EM4 increases in abundance in the palaeosol layers, indicating the deposition of sandy-silty loess during pedogenesis. These results are in contrast with end-member modelling results of typical Chinese loess-palaeosol sequences on the Central Loess Plateau (Prins et al., 2007; Prins and Vriend, 2007; Shang et al., 2017; Vriend et al., 2011), and the sequences along the Yellow River (*NE Tibetan Plateau*: Vriend and Prins, 2005; *Mangshan Plateau*: Prins et al., 2009; Shang et al., 2018). In those loess-palaeosol sequences, the interglacial palaeosol layers demonstrate an increase in abundance of the finest clayey silty end-member (modal grain size ~22 μm), and the glacial loess deposits are dominated by sandy silts with a mode of ~37 and ~63 μm. The dominance of a fine component in palaeosols is explained by a reduced input from 'proximal' sources as a result of weakening of the East Asian Winter Monsoon during interglacial periods.

The coarsening observed in the palaeosol layers of the Baoshan section is a result of non-aeolian depositional and/or erosional processes, most likely related to increased surface runoff triggered by increased precipitation during the interglacial periods. The episodic increase in EM4 abundance could thus be explained by local surface runoff redepositing relatively coarse material eroded from the higher elevated terrace levels or surrounding pediplain surface and/or winnowing (preferential removal) of fine sediment. The poorly-sorted layer containing coarse sand and granules (up to ~3 mm) observed adjacent to profile X and the coarse angular quartzite flakes observed in profile C affirms this interpretation. This is also in agreement with Lei (1998), who concludes that the loess deposits in the Qinling Mountains are fragmentary because of erosional processes.

The terraces of T3 are very extensive (Fig. 2). The limited infiltration capacity of the fine grained deposits with a high clay content promotes surface runoff processes, as evidenced by the present-day intensive dissection of the T3 surface by gullies (Fig. 2 and detailed in Fig. 15). Combined with the large width of the surfaces, this implies an important contribution to the transport of sediment by surface runoff. This interpretation is in agreement with Yang et al. (2019) as their results also indicate episodic deposition of coarse sediment in aeolian deposits on terrace levels T2 (11 km to the east of the Baoshan section) and T4 (in the west of the Hanzhong Basin). They suggest that this component is deposited by temporary overland flowing water or, alternatively, that it reflects the presence of pedogenic nodules that were not dissolved during the pre-treatment process.

The loess layers between the palaeosols are dominantly composed of EM1, EM2 and EM3 (modal size ~6, 14, 31 μm, respectively). EM1 could be the result of pedogenic clay formation or related to an input of a very fine aeolian component (background sedimentation, cf. Vandenberghe, 2013), or most likely a combination of those two factors. EM2 is comparable with the background sedimentation clayey loess (modal size ~22 μm) and EM3 is comparable with the proximal silty loess (modal size ~37 μm) component of the Central Loess Plateau (Fig. 16, Prins and

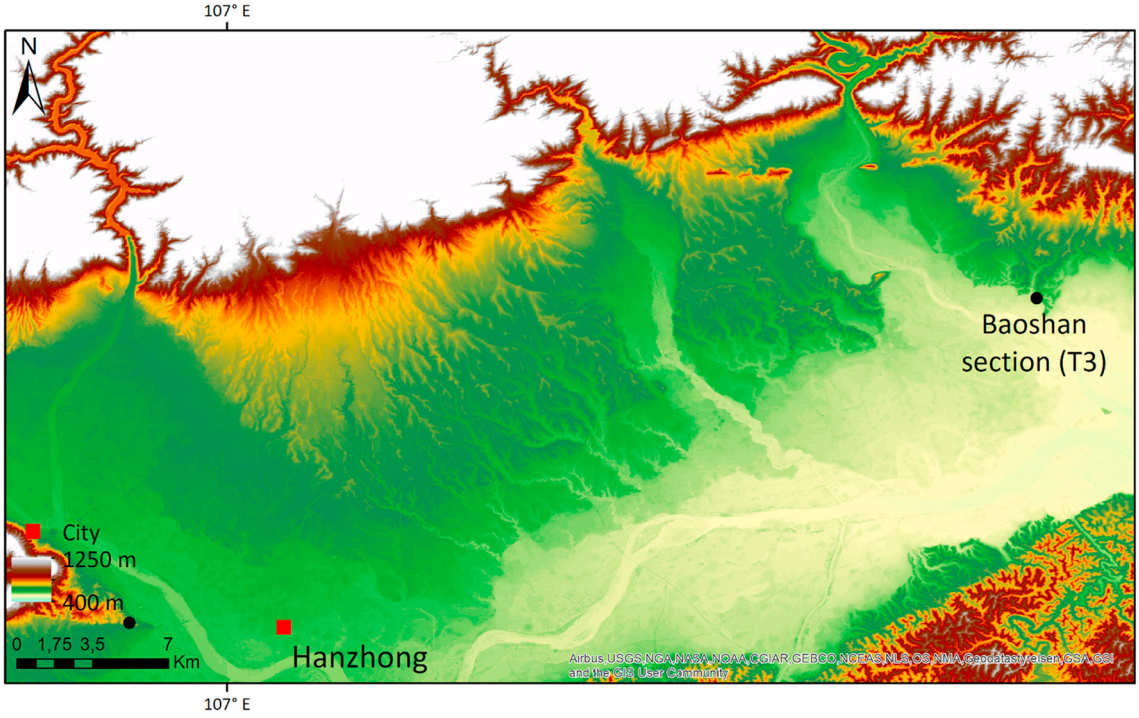

Fig. 15. Digital elevation model (DEM) of the terraces north of the Hanjiang River. The DEM clearly illustrates the intensive dissection by gullies of the terrace surfaces.

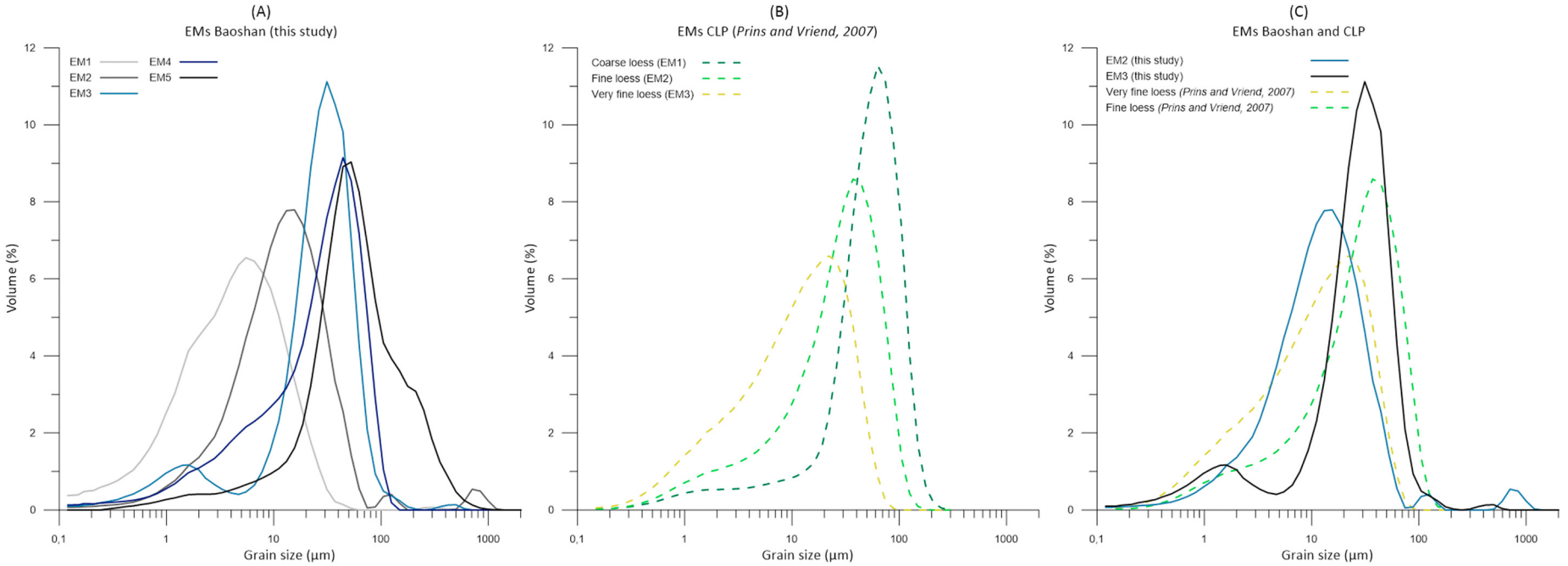

Fig. 16. Comparison of (A) the Baoshan end-member model (this study) with (B) the end-member model of the Late Quaternary loess-palaeosol sequences from the Central Loess Plateau (CLP) of Prins and Vriend (2007). C) End members EM3 and EM2 of the Baoshan model (modal size 31 and 14 µm respectively) show striking similarities with EM2 and EM3 of the CLP model (modal size 37 and 22 µm respectively).

Vriend, 2007). This resemblance affirms our interpretation of the silty deposits as being of an aeolian origin.

The particle count data obtained with dynamic image analysis validates the end-member modelling results, which are based on laser-diffraction grain size analysis (Fig. 10). Increased particle counts >20 μm occur at similar depth intervals as the increased abundances of EM4 in the palaeosol layers. Furthermore, the total particle counts and sand fraction show a similar upward decreasing trend in the lower 6.5 m of the composite section, which mirrors the fining-up trend reflected by the end-member abundances. Average sand counts in the fluvial part (27–20.5 m depth) is 36×10^3, while in the loess deposits it is 11×10^3.

The aspect ratio of all profiles shows a decreasing trend with increasing grain size, illustrating increased elongation for coarser particles (Fig. 11). These results are analogous with the results of Shang et al. (2017), who applied dynamic image analysis on loess deposits of the Central Loess Plateau. They conclude that the decreasing aspect ratio with increasing grain size is related to systematic shape sorting during aeolian transport and is, therefore, a fingerprint for suspension transport processes of primary Chinese loess. A similar size-shape trend is observed in the upper 20.5 m of the Baoshan section, strengthening the interpretation that this interval is composed of aeolian deposits. It seems that the grain shape characteristics are not affected by the surface runoff processes. Although the fluvial deposits at the base of the Baoshan section (profile D) show a similar shape-size trend; profile E is characterized by overall significantly lower aspect ratios. Similar findings are reported in Yang et al. (2019), where it is shown that fluvial deposits have slightly lower aspect ratios with relatively large variations compared with the loess deposits.

5.3. Age model of the Baoshan sequence: Implications for fluvial dynamics in the Hanzhong Basin

Two subgroups (A and B) are present in the terrestrial cosmogenic nuclide (TCN) burial dating results. Based on the linear regression of measured ^{26}Al and ^{10}Be concentrations and calculations of isochron-burial ages following Granger (2014), subgroup A should be excluded because of previous (potentially multiple) burial histories. Subset B indicates an isochron-burial age for the terrace gravels of 0.6 ± 0.14 Ma.

Combining all evidence (field observations, grain size and shape characteristics and end-member modelling results) it is concluded that the Baoshan section is composed of fluvial fining-up deposits of 9.5 m in thickness that are overlain by a 20.5 m thick loess-palaeosol sequence, comprising five distinct palaeosol layers. Pedostratigraphic correlation with the loess-palaeosol sequences from the Central Loess Plateau, with ages of the palaeosol-loess boundaries derived from Heslop et al. (2000), results in the age model presented in Fig. 17. Because of the intensely weathered characteristic of the section, it is unknown if the lower boundaries of the thick palaeosol layers represent the transition from a glacial to an interglacial period; the soils may have partly formed in pre-existing glacial loess deposits. Therefore, we decided to only use the age estimates of the top of the palaeosol layers in our age model.

The oldest palaeosol layer, between 17 and 13.2 m, is correlated to S5 (0.625–0.503 Ma). Consequently, the underlying loess layer is correlated with L6. Therefore, the transition from a fluvial to an aeolian environment occurred between 0.625 and 0.693 Ma (upper and lower boundary L6). The correlated age is consistent with the age derived from TCN burial dating. The overlying four palaeosol layers are correlated with S4, S3, S2 and S1, respectively. This correlation fits well with the age model proposed by Sun et al., 2017b. In their results, loess deposits on terrace T3 are pedostratigraphically correlated with S1 to S5 with absolute dates provided by TT-OSL dating of S1, L2 and S2 supporting their age model.

In previous research, the distinction of the fluvial and aeolian environment is merely based on observations and the presence of palaeosol and loess-like layers (Lu et al., 2011a, 2011b; Zhang et al., 2012; Sun et al., 2013, 2014, 2017b; Fang et al., 2017). With our approach, we can objectively pinpoint the exact depth of the transition from a fluvial to an aeolian environment. This contributes to the chronology and natural environment reconstructions for hominins. In the Baoshan section, two artefacts are found in slumped blocks originating from the top of the section (Fig. 18). The artefacts were present in the loess deposits. At other T3 terrace remnants, artefacts are found at the surface and excavated at the base of the loess deposits (within S5, Sun et al., 2012, 2017b). The work of Yang et al. (2019) demonstrates that artefacts on terrace levels T4 and T2 are found in aeolian deposits but also, although less frequent, in fluvial deposits, indicating that both environments provided favourable living conditions. Their work emphasizes the mportance of making the distinction between those sedimentary environments and the subsequent implications for reconstructions of palaeo-environmental living conditions for hominins.

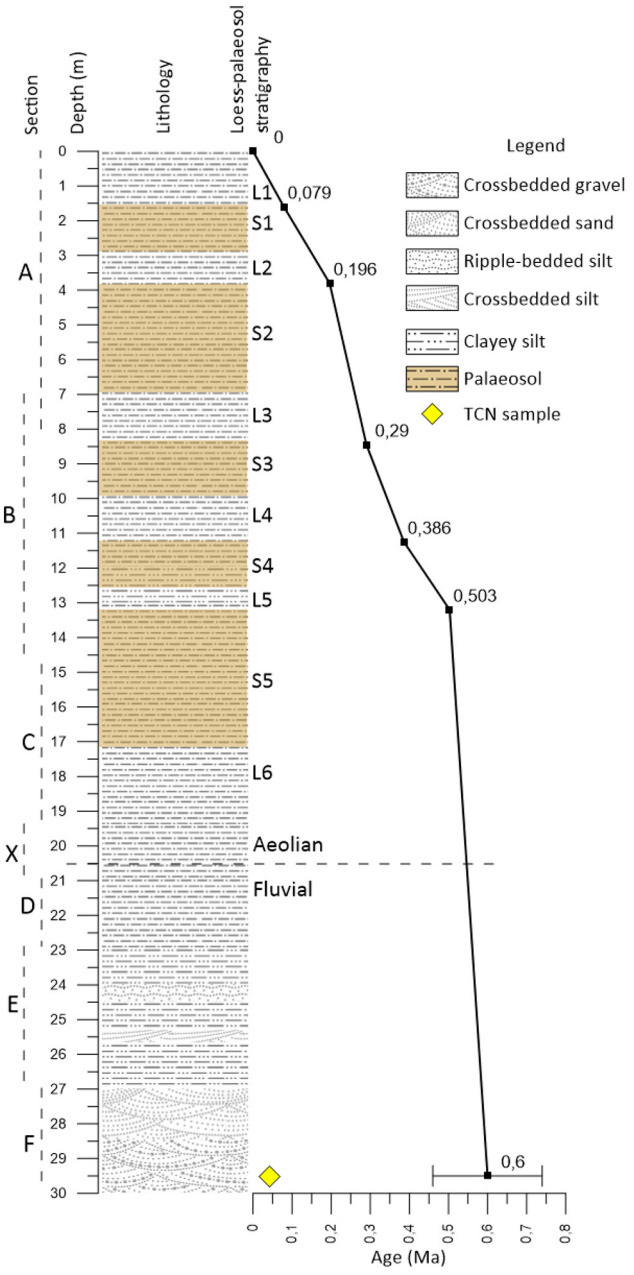

Fig. 17. Age model for the Baoshan section, illustrating the loess-palaeosol stratigraphy. The ages of the upper boundaries of the palaeosol layers are derived from Heslop et al. (2000). The boundary between the fluvial and aeolian deposits is present at 20.5 m.

Fig. 18. Two artefacts found in slumped blocks of the Baoshan section.

The age of the fluvial-aeolian facies transition and the age of the terrace gives insight in the fluvial morphodynamics of the Hanjiang River. The terrace level is abandoned between 0.625 and 0.693 Ma indicating incision of the Hanjiang River during this period. This observation, combined with the abandonment age estimate of terrace level T2 of ~0.1 Ma (Sun et al., 2017b), implies a long period (~0.53–0.59 Ma) of fluvial stability and aeolian dust deposition on terrace level T2.

The terrace abandonment ages roughly correlate with uplift episodes, related to uplift of the Tibetan Plateau and movement of India towards Asia, of the QLM at 0.6 and 0.15 Ma. Similar ages are obtained for terraces in the Luonan Basin (Fang et al., 2017). This suggest that the incision of the Hanjiang River, resulting in the abandonment of the terraces, are the result of tectonically-forced base-level drop. Subsequently, the shift from a fluvial to an aeolian depositional environment, and the coherent shift in the natural living conditions for hominins are tectonically forced.

6. Conclusions

This study focuses on a homogenous, fine grained (mainly fine silt- to clay-sized), sedimentary sequence at Baoshan in the Hanzhong Basin, an intramontane basin located in the Qinling Mountains, central China. Because of incision of the Hanjiang River, a terraced landscape with six terrace levels has been formed. The Baoshan section is located in the eastern part of the basin on the third terrace level.

The base of the Baoshan section consists of a fluvial fining up sequence of at least 7 m in thickness. The basal 3 m consist of gravel and coarse sand and 4 m of silts (modal size ~32 μm) at the top. This sequence is overlain by homogenous clayey silt (modal size ~25 μm) deposits of ~23 m in thickness.

End-member modelling of the grain size dataset results in a five end-member model. The coarsest end-member (EM5) represents fluvial sediment rich in sand-sized micas. It is solely present at a depth range of 27–20.5 m. Based on the absence of mica-rich silts and the end-member abundance, and supplemented by the lack of significant grain size variation, lack of other fluvial deposits (channels, bars, etc.), and large thickness of the sequence, it is concluded that the top 20.5 m of the Baoshan section are composed of aeolian deposits.

The end-member mixing coefficients show a coarsening (increase in abundance of EM4) in the palaeosol layers. The coarsening in the palaeosol layers is most likely the result of climatically-forced increases in local surface runoff causing winnowing of fine sediment and/or deposition of relatively coarse material during interglacial periods. Because of the determined depth of the fluvial-aeolian facies transition and the TCN burial dated terrace gravel (0.6 ± 0.14 Ma), pedostratigraphic correlation of the palaeosol layers with the Central Loess Plateau is possible. The oldest palaeosol is correlated with S5 (0.625–0.503 Ma). Therefore, the transition from a fluvial to an aeolian environment took place between 0.625 and 0.693 Ma. This marks the moment of terrace abandonment by incision of the Hanjiang River, which correlates with an uplift episode of the Qinling Mountains.

Acknowledgements

This research is supported by the National Natural Science Foundation of China (41971005, 41522101), the Royal Netherlands Academy of Arts and Sciences (Chinese Exchange Program, grant number 530-5CDP07), and the CAS Strategic Priority Research Program Grant B "Macroevolutionary Processes and Paleoenvironments of Major Historical Biota" (No. XDPB05). We are very grateful and would like to thank Bas Knaake for his assistance and discussions during the fieldwork in 2017. We also would like to thank Martine Hagen for her help in the sediment laboratory of the Vrije Universiteit Amsterdam and Hans van Hateren for his help with the end-member modelling.

Declaration of competing interest

The authors declare that they have no known competing financial interests or personal relationships that could have appeared to influence the work reported in this paper.

References

Akçar, N., Ivy-Ochs, S., Alfimov, V., Schlunegger, F., Cluade, A., Reber, R., Christl, M., Vockenhuber, C., Dehnert, A., Rahn, M., Schlüchter, C., 2017. Isochron-burial dating of glaciofluvial deposits: first results from the Swiss Alps. Earth Surf. Process. Landforms 42, 2414–2425.

Aslan, A., Autin, W.J., 1998. Holocene flood-plain soil formation in the southern lower Mississippi Valley: implications for interpreting alluvial paleosols. GSA Bull. 110 (4), 433–449.

Balco, G., Rovey, C.W., 2008. An isochron method for cosmogenic nuclide dating of buried soils and sediments. American Journal of Sciences 308, 1083–1114.

Balco, G., Stone, J.O., Lifton, N.A., Dunai, T.J., 2008. A complete and easily accessible means of calculating surface exposure ages or erosion rates from 10Be and 26Al measurements. Quat. Geochronol. 3, 174–195.

Binnie, S.A., Dunai, T.J., Voronina, E., Goral, T., Heinze, S., Dewald, A., 2015. Separation of Be and Al for AMS using single-step column chromatography. Nucl. Instr. And Meth. In Phys. Res. B 361, 397–401.

Bronger, A., Winter, R., Sedov, S., 1998. Weathering and clay mineral formation in two Holocene soils and in buried paleosols in Tadjikistan: towards a Quaternary paleoclimatic record in Central Asia. Catena 34, 19–34.

Dunai, T.J., 2010. Cosmogenic Nuclides Principles, Concepts and Applications in the Earth Surface Sciences. Cambridge University Press, Cambridge.

Erlanger, E.D., Granger, D.E., Gibbon, R.J., 2012. Rock uplift rates in South Africa from isochron burial dating of fluvial and marine terraces. Geology 40, 1019–1022.

Fang, Q., Hong, H., Zhao, H., Lu, H., Han, W., Liu, Y., Jia, Z., Wang, C., Yin, K., Algeo, T.J., 2017. Tectonic uplift-influenced monsoonal changes promoted hominin occupation of the Luonan Basin: insights from a loess-paleosol sequence, eastern Qinling Mountains, central China. Quat. Sci. Rev. 169, 312–329.

Feng, J.-L., Hu, Z.-G., Ju, J.-T., Lin, Y.-C., 2014. The dust provenance and transport mechanism for the Chendu Clay in the Sichuan Basin, China. Catena 121, 68–80.

Feng, J.-L., Ju, J.-T., Chen, F., Hu, Z.-G., Zhao, X., Gao, S.-P., 2016. Identification of a late Quaternary alluvial-aeolian sedimentary sequence in the Sichuan Basin, China. Quat. Res. 85, 279–289.

Granger, D.E., 2006. A review of burial dating methods using ^{26}Al and ^{10}Be. Geological Society of America Special Publication 415, 1–16.

Granger, D.E., 2014. Cosmogenic nuclide burial dating in archaeology and paleoanthropology. In: Holland, H.D., Turekian, K.K. (Eds.), Treatise on Geochemistry, second edition 14. Elsevier, Oxford, pp. 81–97.

Guo, Y., Huang, C.C., Pang, J., Zha, X., Zhou, Y., Zhang, Y., Zhou, L., 2013. Sedimentological study of the stratigraphy at the site of Homo Erectus Yunxianensis in the upper Hanjiang River valley, China. Quat. Int. 300, 75–82.

He, Q., Walling, D.E., 1998. An investigation of the spatial variability of the grain size composition of flood plain sediments. Hydrol. Process. 12, 1079–1094.

Heslop, D., Langereis, C.G., Dekkers, M.J., 2000. A new astronomical timescale for the loess deposits of Northern China. Earth Planet. Sci. Lett. 184, 125–139.

Konert, M., Beets C.J., internal VU report. Analysis of organic matter and carbonates in sediments with a thermo-gravimetric analyzer (TGA). (Manuscript in preparation).

Konert, M., Vandenberghe, J., 1997. Comparison of laser grains size analysis with pipette and sieve analysis: a solution for the underestimation of the clay fraction. Sedimentology 44, 523–535.

Kraus, M.J., 2002. Basin-scale changes in floodplain paleosols: implications for interpreting alluvial architecture. J. Sediment. Res. 72 (4), 500–509.
Lal, D., 1991. Cosmic-ray labeling of erosion surfaces – in situ nuclide production-rates and erosion models. Earth Planet. Sci. Lett. 104, 424–439.
Lei, X.-Y., 1998. Grain-size analysis and genesis of loess in the Qinling Mountains. Acta Geol. Sin. 2.
Lu, H., Sun, X., Wang, S., Cosgrove, R., Zhang, H., Yi, S., Ma, X., Wei, M., Yang, Z., 2011a. Ages for hominin occupation in Lushi Basin, middle of South Luo River, central China. J. Hum. Evol. 60, 612–617.
Lu, H., Zhang, H., Wang, S., Cosgrove, R., Sun, X., Zhao, J., Sun, D., Zhao, C., Shen, C., Wei, M., 2011b. Multiphase timing of hominin occupations and the paleoenvironment in Luonan Basin, Central China. Quat. Res. 76, 142–147.
Nishiizumi, K., 2004. Preparation of ^{26}Al AMS standards. Nuclear Instruments and Methods Part B 223–224, 388–392.
Nishiizumi, K., Imamura, M., Caffee, M., Southon, J., Finkel, R., McAnich, J., 2007. Absolute calibration of 10Be AMS standards. Nucl. Inst. Methods Phys. Res. B 258, 403–413.
Paterson, G.A., Heslop, D., 2015. New methods for unmixing sediment grain size data. Geochem. Geophys. Geosyst. 16, 4494–4506.
Prins, M.A., Vriend, M., 2007. Glacial and interglacial eolian dust dispersal patterns across the Chinese Loess Plateau inferred from decomposed loess grain-size records. Geochem. Geophys. Geosyst. v8 (7), 1–17.
Prins, M.A., Weltje, G.J., 1999. End-member modelling of siliciclastic grain-size distributions: the Late Quaternary record of aeolian and fluvial sediment supply to the Arabian Sea and it paleoclimatic significance. In: Harbauch, J., et al. (Eds.), Numerical Experiments in Stratigraphy: Recent Advances in Stratigraphy and Sedimentologic Computer Simulations. Society for Sedimentary Geology, Special Publication 62, pp. 91–111.
Prins, M.A., Weltje, G.J., 1999b. End-member modelling of grain-size distributions of sediment mixtures. Prins, M.A., 1999. Pelagic, Hemipalegic and Turbidite Deposition in the Arabian Sea During the Late Quaternary: Unravelling the Signals of Aeolian and Fluvial Sediment Supply as Functions of Tectonics, Sea-level and Climate Change by Means of End-member Modelling of Siliciclastic Grain-size Distributions [Ph.D. thesis]. 168. Utrecht University, Geologica Ultraiectina, Utrecht, pp. 47–68.
Prins, M.A., Vriend, M., Nugteren, G., Vandenberghe, J., Lu, H., Zheng, H., Weltje, G.J., 2007. Late Quaternary aeolian dust input variability on the Chinese Loess Plateau: inferences from unmixing of loess grain-size records. Quat. Sci. Rev. 26, 230–242.
Prins, M.A., Zheng, H., Beets, K., Troelstra, S., Bacon, P., Kamerling, I., Wester, W., Konert, M., Huang, X., Ke, W., Vandenberghe, J., 2009. Dust supply from river floodplains: the case of the lower Huang He (Yellow River) recorded in a loess–palaeosol sequence from the Mangshan Plateau. J. Quaternary Sci. 24, 75–84.
Rost, K.T., 1994. Paeoclimatic field studies in and along Qingling Shan (Central China). GeoJournal 34 (1), 107–120.
Shang, Y., Kaaniken, A., Beets, C.J., Prins, M.A., 2017. Aeolian silt transport processes as fingerprinted by dynamic image analysis of the grain size and shape characteristics of Chinese loess and Red Clay deposits. Sedimentary Geology 1–13.
Shang, Y., Prins, M.A., Beets, C.J., Kaaniken, A., Lahaye, Y., Dijkstra, N., Rits, D.S., Wang, B., Zheng, H., van Balen, R.T., 2018. Aeolian dust supply from the Yellow River floodplain to the Pleistocene loess deposits of the Mangshan Plateau, central China: evidence from zircon U-Pb age spectra. Quat. Sci. Rev. 182, 131–143.
Sun, J., 2005. Long-term fluvial archives in the Fen Wei Graben, central China, and their bearing on the tectonic history of the India-Asia collision system during the Quaternary. Quat. Sci. Rev. 24, 1279–1286.
Sun, X., Lu, H., W, S., Yi, S., 2012. Ages of Liangshan Paleolithic sites in Hanzhong Basin, central China. Quat. Geochronol. 10, 380–386.
Sun, X., Lu, H., Wang, S., Yi, S., Shen, C., Zhang, W., 2013. TT-OSL dating of Longyadong Middle Paleolithic site and paleoenvironmental implications for hominin occupation in Luonan Basin (central China). Quat. Res. 79, 168–174.
Sun, X., Lu, H., Wang, S., Cosgrove, R., Zhang, W., Yu, K., Zhuo, H., 2014. Age of newly discovered Paleolithic assemblages at Liuwan site Luonan Basin, central China. Quat. Int. 347, 193–199.
Sun, X., Li, Y., Feng, X., Lu, C., Lu, H., Yi, S., Wang, S., Wu, S.-Y., 2015. Pedostratigraphy of aeolian deposits near Yunxian Man site on the Hanjiang River terraces, Yunxian Basin, central China. Quaternary International xxx, 1–8.
Sun, X., Jia, X., Lu, H., Wang, X., Yi, S., Wang, X., Xu, Z., Lei, F., Han, Z., 2017a. A modified depositional hypothesis of the Hanjiang Loess in the southern Qinling Mountains, central China. Prog. Phys. Geogr. 41 (6), 1–13.
Sun, X., Lu, H., Wang, S., Yi, L., Li, Y., Bahain, J.J., Voinchet, P., Hu, X., Zeng, L., Zhang, W., Zhuo, H., 2017b. Early human settlements in the southern Qinling Mountains, central China. Quat. Sci. Rev. 164, 168–186.
Tunwal, M., Mulchrone, K.F., Meere, P.A., 2018. Quantitative characterization of grain shape: Implications for textural maturity analysis and discrimination between depositional environments. Sedimentology 65 (5), 1761–1776.
Tysmans, D., Haesaerts, P., Bogemans, F., Claeys, P., Finsy, R., Van Molle, M., 2009. Heterogeneity in homogeneous Brabantian loess during the Late Pleniglacial. Quat. Int. 198, 195–203.
Van Hateren, J.A., Prins, M.A., van Balen, R.T., 2017. On the genetically meaningful decomposition of grain-size distributions: a comparison of different end-member modelling algorithms. Sediment. Geol. 1–23.
Vandenberghe, J., 2013. Grain size of fine-grained windblown sediment: a powerful proxy for process identification. Earth Sci. Rev. 121, 18–30.
Vriend, M., Prins, M.A., 2005. Calibration of modelled mixing patterns in loess grain-size distributions: an example from the north-eastern margin of the Tibetan Plateau, China. Sedimentology 52 (6), 1361–1374.
Vriend, M., Prins, M.A., Buylaert, J.P., Vandenberghe, J., Lu, H., 2011. Contrasting dust supply patterns across the north-western Chinese Loess Plateau during the last glacial-interglacial cycle. Quat. Int. 240, 167–180.
Wang, S., Lu, H., Zhang, H., Sun, X., Yi, S., Chen, Y., Zhang, G., Xing, L., Sun, W., 2014. Newly discovered Palaeolithic artefacts from loess deposits and their ages in Lantian, central China. Chin. Sci. Bull. 59 (7), 651–661.
Weltje, G.J., Prins, M.A., 2003. Muddled or mixed? Inferring palaeoclimate from size distributions of deap-sea clastics. Sediment. Geol. 162 (1–2), 39–62.
Weltje, G.J., Prins, M.A., 2007. Genetically meaningful decomposition of grain-size distributions. Sediment. Geol. 202, 409–424.
Xia, W.T., Wang, S.J., Xia, N., Lu, H., Wang, X., Sun, X., Zhang, H., Zhang, W., Zhuo, H., Xing, L., Yu, Q., Feng, W., 2017. Lithic artifacts excavated from locality 3 of the Longgansi site in Hanzhong Basin, Shaanxi Province (in Chinese with English abstract). Acta Anthropologica Simica 36 (e), 400–412 2017e.
Yang, S., Fang, X., Shi, Z., Lehmkuhl, F., Song, C., Han, Y., Han, W., 2010. Timing and provenance of loess in the Sichuan Basin, southwestern China. Palaeogeogr. Palaeoclimatol. Palaeoecol. 292, 144–154.
Yang, X., Wang, X., van Balen, R.T., Prins, M.A., Wang, S., van Buuren, U., Lu, H., 2019. Fluvial terrace formation and early human settlement in the Hanzhong Basin, Qinling Mountain, central China. Glob. Planet. Chang. 178, 1–14.
York, D., Evensen, N.M., Martinez, M.L., Delgado, J.D., 2004. Unified equations for the slope, intercept, and standard errors of the best straight line. Am. J. Phys. 72, 367–375.
Zhang, H., Lu, H., Jiang, S., Vandenberghe, J., Wang, S., Cosgrove, R., 2012. Provenance of loess deposits in the Eastern Qinling Mountains (central China) and their implications for the paleoenvironment. Quat. Sci. Rev. 43, 94–102.
Zhang, Y., Huang, C.C., Pang, J., Zha, X., Zhou, Y., Gu, H., 2013. Holocene paleofloods related to climatic events in the upper reaches of the Hanjiang River valley, middle Yangtze River Basin, China. Geomorphology 195, 1–12.